Front. Struct. Civ. Eng. 2022, 16(9): 1104–1126
https://doi.org/10.1007/s11709-022-0845-x

RESEARCH ARTICLE

Compressive and cyclic flexural response of double-hooked-end steel fiber reinforced concrete

Demewoz W. MENNA, Aikaterini S. GENIKOMSOU*, Mark F. GREEN

Department of Civil Engineering, Queen's University, Kingston, ON K7L 3N6, Canada
**Corresponding author. E-mail: ag176@queensu.ca*

ABSTRACT Recent developments on high-performance double-hooked-end steel fibers have enhanced the wide applications of steel fiber reinforced concrete (SFRC). This study presents the compressive properties and the cyclic flexural performance of the SFRC that were experimentally examined. Three different double-hooked-end steel fibers at 0.25%, 0.5%, 0.75%, and 1% volume fractions were considered. All fiber types had similar length to diameter ratios, while the first two fiber types had similar anchorage mechanisms (4D) and tensile strength and the third type had different anchorage mechanism (5D) and a higher tensile strength. The increased volumetric ratio of the fibers increased the post-peak compressive strain (ductility), the tensile strength, and the cyclic flexural strength and cumulative energy dissipation characteristics of the SFRC. Among the 4D fibers, the mixtures with the larger steel fibers showed higher flexural strength and more energy dissipation compared to the SFRCs with smaller size fibers. For 1% steel fiber dosage, 4D and 5D specimens showed similar cyclic flexural responses. Finally, a 3D finite element model that can predict the monotonic and cyclic flexural responses of the double-hooked-end SFRC was developed. The calibration process considered the results obtained from the inverse analysis to determine the tensile behavior of the SFRC.

KEYWORDS steel fiber reinforced concrete, fiber geometry, cyclic loading, energy dissipation, finite element modeling, inverse analysis

1 Introduction

Applications of steel fiber reinforced concrete (SFRC) have been growing due to its numerous advantages over conventional reinforced concrete. SFRC enables faster and lower-cost labour construction since the fabrication and the placement of reinforcing bars is eliminated. SFRC also enables elegant structural designs with thinner and complex structural member shapes [1]. The addition of steel fibers improves the post-cracking load carrying capacity, the tensile strength, the flexural toughness, the energy absorption capacity, and the durability [2–5]. Introduction of newly engineered steel fibers (with more effective anchorage and higher strength) to the market enabled fabrication of SFRC with superior performance. However, more information is required on the effect of anchorage and volume fraction of double-hooked-end fibers on the compressive, cyclic flexural property and finite element modeling of SFRC fabricated with these new types of fibers.

Article history: Received Oct 26, 2021; Accepted Mar 21, 2022

2 Scope and significance

To address the lack of experimental data, this paper reported results on the flexural behaviour of double-hooked-end SFRC under cyclic loading. The effects of volumetric ratio of three different types of double-hooked-end fibers with similar aspect ratios on the compressive stress-strain relationship, tensile strength and cyclic flexural resistance are investigated. The novelty of the present work lies on the high level of mechanical anchorage and tensile strength of the double-hooked-end steel fibers. The additional anchorage increases the pullout resistance and higher energy will be dissipated by the plastic deformation (straightening) of the end-hooks. The findings of this study provide a better understanding of the energy dissipation characteristics under repeated

loading that are necessary for widespread application of the double-hooked-end fibers that have been recently added to the market. In this study, surface crack propagation and transverse strain of prisms under cyclic loading are examined using digital image correlation (DIC). DIC is an optical non-contact technique that uses successive real-time digital images with random patterns (speckles). The field displacement is measured by comparing a small subset on an image taken prior to deformation to a corresponding subset on an image taken after deformation [6]. DIC avoids rigid body motion, enables a high-resolution measurement of surface deformation, and doesn't require to pause running tests for marking cracks (which is useful in cyclic tests). DIC method has been successfully used in various experimental research including flexural cracking investigation in concrete prisms [7], mechanical performance of strengthened reinforced concrete beams in monotonic and cyclic loading under four-point bending [8,9] and full-scale testing of prestressed concrete structures [10]. This technique was also successfully implemented to study cracking behaviour of SFRC during splitting tensile [11] and flexural tests [12].

3 Literature review

Structural performance of SFRC under monotonic and cyclic loading depends on the geometry, distribution, and volume fraction of the fibers, and the bond strength between the matrix and fibers [13]. The fiber volumetric ratio is a key parameter to determine the compressive, tensile, and post-cracking flexural properties of SFRC. Although the increase in the volume content of fibers decreases the workability of SFRC, the addition of higher dosage of fibers significantly enhances the splitting tensile, flexural and compressive strengths of the mixture [14]. Yoo et al. [15] used single-hooked-end fibers with fiber content of 1.0% and 2.0% by volume of mixture that increased the ultimate flexural resistance by 13% and 63%, respectively when compared to concrete without fibers. Similarly, the deflection corresponding to the ultimate flexural load increased with the increase of fiber content leading to a more ductile failure. The 28 d compressive strength and the modulus of elasticity of regular concrete are slightly affected by the addition of fibers. The maximum increase in compressive strength and the modulus of elasticity due to the addition of fibers up to 1.5% by volumetric ratio of concrete is found to be less than 10% [16]. However, the axial strain-softening behaviour in compression and the toughness are highly improved by introducing more steel fibers to the mixture [17].

Aspect ratio (L_f/D_f, where L_f denotes the fiber's length and D_f is the fiber's diameter) is one of the most important properties of the fibers, since it can influence the fiber distribution and the workability of the mix. The common aspect ratios of steel fibers available in the market vary between 50 to 100 [14,18]. Both the flexural and split tensile strengths of the SFRC increase with an increase in the aspect ratio. This increase in the mechanical properties attributed to the improvement of heterogeneous distribution and flocculation of fibers with the increase in aspect ratio [14]. Moreover, Han et al. [19] concluded that the ratio of steel fiber length and maximum aggregate size significantly affected splitting tensile, flexural performance and fracture characteristics of SFRC.

The interfacial bond and anchorage between the fibers and the matrix plays a significant role in the capacity of the fibers to transfer the applied stresses in cracked concrete. Weaker bond strength between matrix and concrete leads to the pullout of the fibers and limits their reinforcing contribution, while too high bond results to fibers' fracture before being able to contribute to the post-cracking strength [20]. Mechanical anchorage is one of the main methods used to improve the pullout resistance of steel fibers from the cementitious matrix. Among the different types of steel fibers, end hook fibers are commonly used due to their advantage to gradually straighten prior to significant slippage [21]. New double-hooked-end steel fibers have been recently released to the market. These fibers were engineered to provide high mechanical anchorage and tensile strength for better structural performance. Abdallah and Fan [20] studied the anchorage mechanism of single and double-hooked-end fibers by conducting pullout tests. The double-hooked-end fibers showed 50% and 25% higher maximum pullout load and total pullout work, respectively, than the corresponding single-hooked-end fibers. As a result, these recently developed double-hooked-end fibers are recommended to improve the mechanical properties for regular and high strength concrete. Previous research has proved that double-hooked-end fibers exhibited enhanced structural performance over single-hooked-end fibers. Results from uniaxial tensile tests on self-compacting concrete with various end-hook steel fibers showed that double-hooked-end fibers demonstrated significantly higher peak and post peak response than single-hooked-end fibers [22]. Chanthabouala et al. [5] experimentally examined the punching shear strength of double-hooked-end SFRC slabs and compared the results with single-hooked-end fiber reinforced concrete. The results showed that at 1.2% volume fraction double-hooked-end fibers can increase the punching shear resistance by 110% to 156% which is significantly higher than the 35% to 65% increase by conventional single-hooked-end fibers. Compressive and cyclic flexural properties of concrete mixtures with double-hooked-end fibers need to be investigated for a wider application of these fibers.

Performance of concrete structures under seismic loading highly depends on the ductility and cumulative energy dissipation characteristics of the structural members [23]. The steel fibers in SFRC improve the ductility and help the structure dissipate the energy induced by earthquake [24]. Although the flexural performance of SFRC under monotonic loading has been studied by various researchers, very limited data exist under cyclic loading [25]. Chalioris et al. [26] reported that steel fibers at 1% to 3% volume fraction dosage significantly improved cyclic flexural response of slender concrete beams with longitudinal bars by enhancing absorbed energy, ductility, crack limiting capability, and damage prevention. Naghibdehi et al. [27] investigated the effects of steel and Polypropylene (PP) fiber reinforced prisms under reverse cyclic loading. Their results showed that increasing hooked-end steel fiber volume fraction from 0.5% to 1.5% doubled energy dissipation capacity after 44 reverse cyclic load steps. However, they reported that SFRC with 2% steel fibers showed slightly lower energy dissipation than SFRC with 1.5% steel fiber. Recent developments on high-performance steel fibers also require the evaluation of the flexural strength under cyclic loading. Understanding the cyclic flexural performance of SFRC is crucial to estimating the energy-absorption, damage evolution, crack propagation and deflection caused by repeated loads [24,28]. Thus, cyclic flexural tests provide us with some material parameters for the design of structural members under service and seismic loads.

To supplement the experimental findings with the objective to further examine the behaviour of SFRC, nonlinear finite element analysis (FEA) can be considered as an advantageous tool. Although there are various constitutive models for plain concrete available in different FEA software, there are limited models for SFRC and a consensus on finite element modeling parameters is not reached for SFRC. Among the limited work, recent studies attempted discreetly representing steel fibers and defining the interface with concrete [29,30]. Bitencourt Jr et al. [31] modeled SFRC as a composite made of concrete, discrete discontinuous fibers and fiber-matrix interface. The steel fibers were modeled as two-node finite elements with elastoplastic constitutive behaviour and the quasi-brittle behaviour of the concrete and fiber-matrix interface were simulated with continuum damage models. Alternatively, plasticity-based constitutive models that consider FRC as a homogeneous material were developed [32–34]. Huo et al. [32] proposed a model that combines plasticity-based smeared crack for concrete and ideal elastic-plastic model for steel. The proposed constitutive model accounts for the inclination and distribution of fibers. Although the aforementioned models appear to closely predict the SFRC mechanical properties under the loading conditions they were evaluated, user defined material subroutine code is required to use them in commercially available software. This could create convergence and compatibility problems that limit the application of the methods [35]. In this research, an existing model for normal concrete, the concrete damage plasticity model, which is available in ABAQUS software is used to simulate the flexural response of fiber reinforced concrete prisms. The compressive stress-strain relationship of the FRC is adopted from the experiments on the cylindrical specimens. The tensile constitutive law is determined from the simplified inverse analysis of four-point flexural prism tests for tension hardening FRC according to CSA S6:19 [36]. The FEM presented in this paper can reproduce both the flexural load deflection responses and crack patterns of the double-hooked-end SFRC, providing an excellent tool for future parametric studies.

4 Experimental program

An experimental investigation was conducted on prisms and cylindrical specimens of plain concrete and SFRC. Thirteen different batches of concrete: one control mix without steel fibers and twelve SFRC mixes with different fiber types and volumetric ratios were prepared. The concrete mix design was prepared based on Kosmatka et al. [37] and the mixture composition is presented in Table 1. General use Portland-Limestone (GUL) type cement that met the standards of the Canadian Standards Association (CSA) A3001 and ASTM C595 with water to cement ratio equal to 0.5 was used. Natural coarse aggregates with a maximum size of 9.5 mm and natural sand fine aggregate were used. Superplasticizer (SP) was added for workability. Three different double-hooked-end steel fibers (named as 4D and 5D according to the manufacturer) with similar aspect ratios (65) were examined. The geometry and the tensile strength of the fibers used in this research are shown in Table 2. The first two types of fibers (named as type A and type B) had similar double-hook anchorage shape and tensile strength (1850 MPa) but different length and diameter while the third fiber (named as Type C) had similar length and diameter with fiber type B but different end-hook geometry and tensile strength. All fibers were bundled with a water-soluble glue that can be easily dispersed prior to mixing. Fiber volume fractions (V_f) of 0% (control specimen), 0.25%, 0.5%, 0.75%, and 1.0% by volume of concrete were investigated for the three types of fibers. The equivalent fiber dosages were 0, 19.5, 39.0, 58.5, and 78.0 kg/m^3 of concrete, respectively. The mixing procedure started by mixing the water with the SP, then, the sand and the coarse aggregates were placed into the mixer with half of the water content. The cement and the remaining water then were added and

Table 1 Concrete mixture proportion and slump test results

mixture	steel fiber		batch weight (kg/m^3)					SP* (mL)	slump (mm)
	type	V_f (%)	cement	water	gravel	sand	fiber		
CS	–	–	456	228	768	891.3	–	–	120
FRCA0.25	A	0.25	456	228	766	886.7	19.5	20	120
FRCA0.5		0.50	456	228	764	882.1	39.0	23	130
FRCA0.75		0.75	456	228	762	877.5	58.5	25	130
FRCA1		1.00	456	228	760	873.0	78.0	28	125
FRCB0.25	B	0.25	456	228	766	886.7	19.5	20	135
FRCB0.5		0.50	456	228	764	882.1	39.0	23	130
FRCB0.75		0.75	456	228	762	877.5	58.5	25	135
FRCB1		1.00	456	228	760	873.0	78.0	28	125
FRCC0.25	C	0.25	456	228	766	886.7	19.5	20	135
FRCC0.5		0.50	456	228	764	882.1	39.0	23	135
FRCC0.75		0.75	456	228	762	877.5	58.5	25	130
FRCC1		1.00	456	228	760	873.0	78.0	28	135

*Note: SP denotes the Superplasticizer.

Table 2 Types of steel fibers used

fiber type	end hook	length, L_f (mm)	diameter, D_f (mm)	L_f/D_f	tensile strength (MPa)
A	double-4D	36	0.55	65	1850
B	double-4D	60	0.90	65	1850
C	double-5D	60	0.90	65	2300

mixed until the mix was homogeneous. Finally, the steel fibers were gradually sprinkled by hand and mixed to get the final mixture. For each mixture group, three prisms with dimensions of 76 mm × 76 mm × 292 mm for cyclic flexural tests and nine 100 mm × 200 mm cylindrical specimens for compressive and splitting tensile strength were cast. The specimens were removed from the mould after 24 h and cured in water for more than 27 d at a temperature of (23 + 5) °C. After 28 d age the specimens were cured in shade until the test day. To study the mechanical properties at 28 d of age, the compressive and tensile strength tests were performed at 28 d. The contribution of the fibers was reported to be significant at later age, thus the prisms were tested at 90 d age. In addition, the compressive strength at 90 d age was also tested.

The compressive and tensile strength tests were carried out on cylindrical specimens with 100 mm × 200 mm dimensions, using a hydraulically operated FORNEY machine with 2000 kN load capacity. As it was mentioned above, the compressive strength tests were conducted at 28 and 90 d age. A compressive stress rate of 0.25 MPa/s was used according to ASTM C39/C39M-20 [38]. The axial deformation was recorded using two linear potentiometers (LP) attached on opposite sides of the compressive cylinder over a gauge length of 127 mm. The modulus of elasticity was determined from the stress-strain relationship according to ASTM C469/C469M-14 [39], that considers 0% to 40% of compressive strength. The tensile strength of the specimens was measured using splitting tensile tests according to ASTM C496/C496M-17 [40] standard at the 28th day age.

4.1 Cyclic flexural test setup and loading protocol

The SFRC prisms were tested under four-point bending according to ASTM C1609 [41]; the test setup is shown in Fig. 1. A 250 kN testing machine (INSTRON 8802) was used for all flexural tests. The prisms were supported by two roller bearings one free to move and the other fixed. The net mid-span deflection of the specimens was measured relative to the centre of the specimen using LP placed on one side. To avoid the effects of seating or

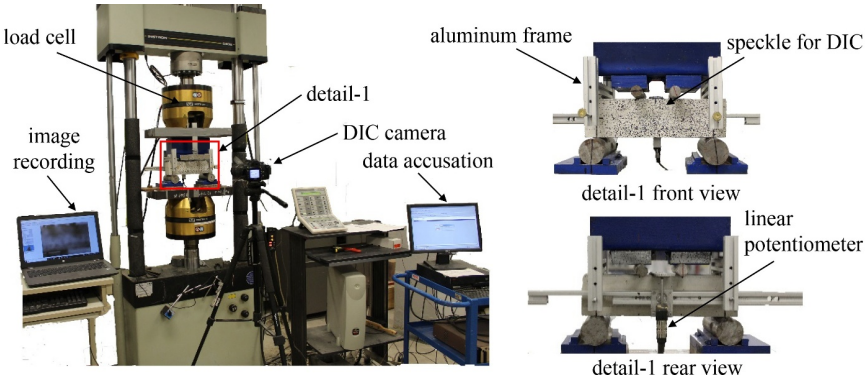

Fig. 1 Cyclic flexural test setup.

twisting of prisms at the supports, an aluminium frame connected to the prism at the mid-depth directly above the supports and pinned to the bar holding the LP was used (Fig. 1, detail 1). DIC technique was also used to measure the formation and the propagation of all developed cracks. Random speckle patterns were applied on one face (the face opposite to the location of LP) and a digital DSLR camera was used to take successive images of the surface. DSLR Remote Pro software (Breeze Systems, Camberley, UK) was employed to precisely monitor the quality, storage and duration between the successive images.

Displacement control loading with a rate of 0.6 mm/min for both loading and unloading was conducted. The cyclic loading protocol is shown in Fig. 2. The loading protocol has 9 displacement cycles starting at 0.25 mm and with an incremental increase of 0.5 mm. The cycles were chosen to enable the measurement of flexural properties under quasi-static repeated loading. The maximum displacement according to the loading protocol was equal to 4.25 mm. After completing all 9 cycles, the loading continued to be applied until the net deflection hit 6 mm, to determine the residual strength.

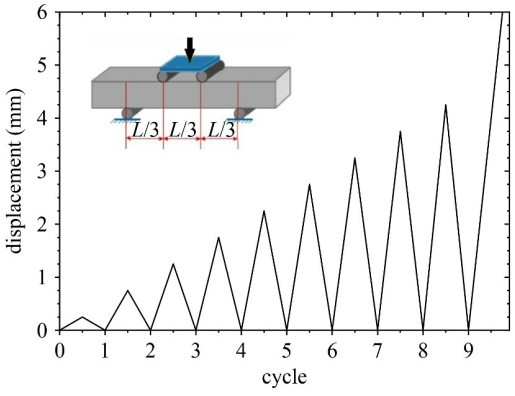

Fig. 2 Loading protocol.

5 Results and disscusion

5.1 Mechanical properties

5.1.1 Compressive and tensile strengths

The compressive and tensile strength test results are summarized in Table 3, where SD represents the standard deviation between specimens of similar mixture composition. Three cylindrical specimens at 28 d age and three specimens at 90 d age were tested under compression for each mixture. Similarly, three cylindrical specimens under splitting tensile were tested to determine the 28 d tensile strength. The smaller values of standard deviation and consistency of stress-strain responses show that the mixtures were cohesive. The majority of the mixtures containing steel fiber type A and B showed slightly lower compressive strength (f_c) at the 28th day than the corresponding control specimen without fibers. Mixtures with steel fibers type A and B at volume fraction up to 0.75% showed a reduction in the compressive strength less than 8.5%. While steel fiber type A with 1% volume fraction resulted to the maximum reduction, about 16%. Similar reduction in the compressive strength was also reported by other studies [13,25] on SFRC with single-hooked-end fibers. This reduction of compressive strength attributed to the orientation of fibers in cylindrical specimens, local stress concentration around the fiber, insufficient compaction and introduction of voids [42]. Up to 10% increase in the 28 d compressive strength was recorded in the specimens with 1% steel fiber type B and in all mixtures with steel fiber type C. At the 90 d of age, all SFRC mixtures showed higher compressive strength than the control specimen without fibers. The average increase at the 90 d age compressive strength due to the addition of 1% volume fraction of steel fiber types A, B, and C was found to be about 19%, 13%, and 24%, respectively. This increase in compressive strength was attributed to the improvement of anchorage between the matrix and fibers as the matrix strength increases during the hydration process.

Unlike the compressive strength, the addition of fibers in concrete significantly increased the tensile strength (f_t')

Table 3 Compressive and tensile strength test results (SD represents standard deviation)

mixture	28th d compression		90th d compression		28th d splitting tension	
	f'_c (MPa)	SD (MPa)	f_c (MPa)	SD (MPa)	f_t (MPa)	SD (MPa)
CS	38.9	0.4	39.5	0.5	4.3	0.4
FRCA0.25	36.6	4.1	45.2	3.3	4.9	0.6
FRCA0.5	37.7	1.7	46.1	1.8	5.9	0.1
FRCA0.75	36.0	2.6	47.5	3.4	6.3	0.0
FRCA1	32.7	3.4	47.1	3.4	6.7	0.1
FRCB0.25	36.4	3.2	50.9	1.4	5.4	0.2
FRCB0.5	35.6	3.7	47.7	2.0	5.5	0.1
FRCB0.75	36.9	6.0	47.2	0.9	5.8	0.4
FRCB1	43.0	1.7	44.5	3.1	8.1	0.5
FRCC0.25	43.0	3.1	43.5	1.4	5.1	0.4
FRCC0.5	43.1	1.3	45.7	3.5	5.8	0.1
FRCC0.75	43.4	1.1	46.8	4.4	6.4	0.5
FRCC1	43.2	5.5	48.9	1.4	7.8	0.2

of the mixtures. As presented in Table 3, increasing the fiber content from 0.5% to 1.0% by volume of concrete, resulted in 37% to 56% increase in the tensile strength for steel fiber type A and 28% to 88% increase in the tensile strength for steel fiber type B. Similarly, by adding 0.5% and 1% (by volume of concrete) steel fiber type C the tensile strength increased by 35% and 81%, respectively. Previous research reported that the increase in splitting tensile strength from adding similar aspect ratio (L_f/D_f= 65) single-hooked-end fibers (V_f = 1%) on normal strength concrete is between 20% and 40% [11,14,16]. This shows that the increase in tensile strength from the addition of double-hooked-end steel fibers (used in this research) is significantly higher than that obtained with the corresponding dosage of single-hooked-end fibers. The splitting tensile strength among the three different fibers showed small variation for volume fractions less than 1%. However, at fiber dosage of 1% by volume fiber types B and C (longer and thicker fibers) showed significantly higher splitting tensile strength than that obtained with fiber type A (shorter and thinner fibers).

5.1.2 Stress-strain behaviour in compression

When steel fibers are added in concrete, both the strain corresponding to the peak compressive stress (ε_{cf}) and the strain at ultimate stress (ε_{uf}) are increased. Typical compression stress−strain curves at 28 d age are presented in Fig. 3. In the majority of the SFRC specimens, the average strain at peak stress (ε_{cf}) increased with an increase in fiber dosage. After the peak stress, SFRC showed a more extended softening branch than plain concrete. In all the three fiber types, the mixture with 1% fiber volume showed a pronounced post-peak stress softening, maintaining about 60% of the compressive strength at a strain value of 0.001. For most of the mixtures, the modulus of elasticity slightly increased with the increase in percentage fraction of steel fibers.

SFRC specimens with a higher dosage of steel fibers showed a more ductile failure. For the purpose of this study compressive failure is defined as the last point in the test and for FRC specimens, the last point corresponds to a stress value equal to around 50% of the ultimate stress. Figure 4 shows the compressive failure patterns of the specimens together with the corresponding values of failure strain (ε_{uf}) and failure stress (f_{uf}). At failure, single major diagonal (shear) cracks were observed in the lesser fiber dosage specimens. Whereas multiple cracks (in the direction of the compressive stress) were observed on cylindrical specimens with a higher volume of fibers. This was mainly due to the contribution of the fibers to produce more ductile failure by resisting growth and propagation of cracks and providing confinement.

5.1.3 Comparison between experimental results and analytical models

Several methods have been proposed to predict the stress-strain relationship of SFRC in compression. Comparison of the present experimental results and proposed models from selected previously published models for 28 d age SFRC in compression and tension are shown in Fig. 5. The models were derived from regression analysis of extensive experimental results by their respective authors [16,43–45]. The first three models [16,44,45] predict mechanical properties of SFRC based on compressive strength of plain concrete and reinforcing index (RI) of the fibers, while the last model [43] considers the experimental compressive strength results of SFRC rather than plain concrete. Details of equations of these models

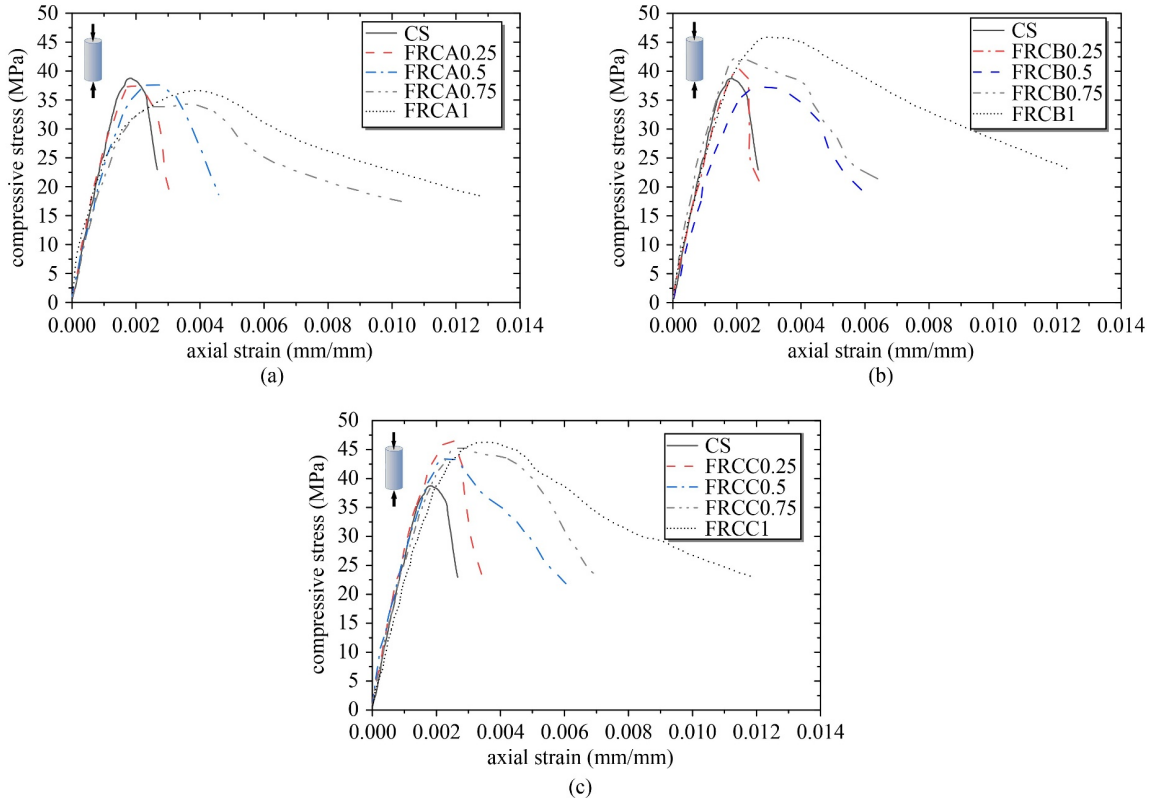

Fig. 3 Typical stress-strain response of SFRC cylinders under compression at 28 d age: (a) fiber type A; (b) fiber type B; (c) fiber type C.

Fig. 4 Failure patterns of the specimens after compression test (the f_{uf} values are in MPa units).

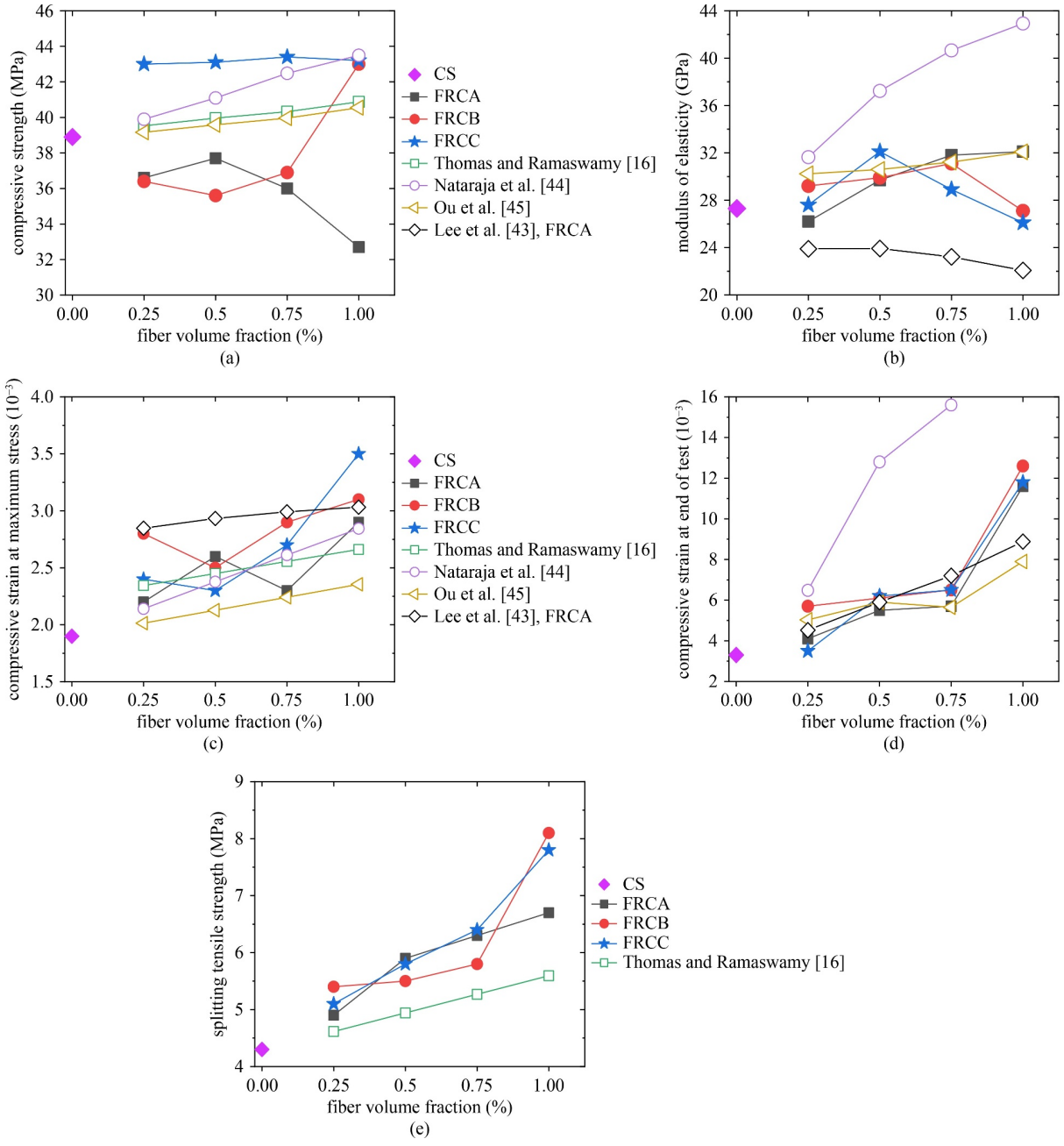

Fig. 5 Average 28 d age experimental results and comparison with previous research model predictions for: (a) compressive strength; (b) modulus of elasticity; (c) compressive strain at maximum stress; (d) compressive strain at end of test; (e) splitting tensile strength.

are presented in the Appendix. The models seem to overestimate most of the compressive strengths of FRCA and FRCB while they seem to underestimate the compressive strengths of the FRCC specimens, Fig. 5(a). The models from Thomas and Ramaswamy [16] and Ou et al. [45] showed relatively closer predictions of strain at peak compressive stress of SFRC specimens, Fig. 5(c). Model from Ou et al. [45] predicted the modulus of elasticity better than the other models. Nataraja et al. [44] seem to overestimate most of the strain at the end of compression test (ε_{uf}) values, Fig. 5(d). Predictions from Lee et al. [43] represent the better compressive strain at the end of the compression test (ε_{uf}) than the other models, Fig. 5(d). As shown in Fig. 5(e), splitting tensile strength prediction from Thomas and Ramaswamy [16] underestimated the experimental results of all the FRC mixtures by a significant margin. Summary for the average standard deviation between the experiment and model predictions is presented in Table 4. In Table 4, f'_c, ε_{co}, f'_{cf}, and ε_{cof} denote the plain concrete peak compressive stress, plain concrete strain at peak compressive stress, SFRC peak compressive stress and

Table 4 Summary of the average standard deviation between model prediction and experimental results

model	average standard deviation between model and experiment				
	f'_{cf} (MPa)	ε_{cof} (10^{-3})	ε_{uf} (10^{-3})	E_{cf} (GPa)	f'_{tf} (MPa)
Thomas and Ramaswamy [16]	2.51	0.16	–	7.01	0.73
Nataraja et al. [44]	2.67	0.18	7.74	6.22	–
Ou et al. [45]	2.50	0.35	1.09	1.49	–
Lee et al. [43]	–	0.25	0.95	3.70	–

SFRC strain at peak compressive stress, respectively. A more comprehensive model in future research is needed for wider application of double-hooked-end SFRC.

5.2 Flexural response under cyclic loading

Typical hysteresis responses of the tested specimens under cyclic loading are shown in Fig. 6. The fibers start being effective after the first crack formation and enable SFRC to be ductile; while the plain control specimen suddenly fails at a very small deflection (0.05 mm) as shown in Fig. 6(g). At the initial cycles, the SFRC prisms were in the elastic range and the area under the hysteresis was small. On subsequent cycles, the specimens entered to the elastic-plastic region and the area under the hysteresis curves was increased with the formation of multiple cracks. Following that, the material damage progressed while the peak load corresponding to each cycle gradually started to decline and the residual deformation started to accumulate. The slope of loading and unloading path decreased with the increased number of cycles; this stiffness degradation was attributed to material damage [25]. For all the three fiber types, addition of more fibers significantly increased the maximum load in each cycle as shown in Fig. 6. The residual displacement is defined as the displacement corresponding to the zero load after unloading. As the number of cycles increased, the residual displacement and residual strain rose. The cyclic hysteretic responses show that, after the first crack formation, the increase in residual displacement was approximately equal to the increase in displacement.

The ultimate flexural strength (f_u, MPa) can be determined using Eq. (1). In Eq. (1), P_u denotes the peak load (in N) and L, b, and d denote clear span, width, and depth of the prism in mm, respectively.

$$f_u = \frac{P_u L}{bd^2}. \quad (1)$$

For all three types of fibers, the ultimate flexural strength of SFRC increased with an increase in the fiber volumetric ratio. Plots for the average ultimate flexural strength versus the fiber dosage are shown in Fig. 7. The addition of 0.25% fiber dosage (for all fiber types) doesn't significantly alter the ultimate flexural strength when compared to the mixture without fibers. At the fiber volumetric ratio of 0.5%, all three fibers showed a similar response; only fiber type C showed slightly a higher ultimate flexural strength compared to the other mixtures. The improvement in ultimate flexural strength compared to the control specimen was 13%, 10%, and 18% for FRCA0.5, FRCB0.5, and FRCC0.5 mixtures, respectively. At 0.75% fiber dosage, the contribution of steel fiber C is significantly higher than that of fiber A and C. The increase in ultimate flexural strength for 0.75% steel fiber A, B, and C was 20%, 33%, and 48%, respectively. At 1% fiber dosage, fiber type B and C showed similar responses, around 94% increase in flexural strength. These strength increases are considerably higher than the 35% to 40% increase in flexural strength from 1% by volume of similar length and aspect ratio single-hooked-end fibers reported in previous research [14]. The results align with remarkable splitting tensile strength improvement from double-hooked-end steel fibers. On the other hand, 1% volume fraction fiber type A showed a 41% increase in flexural strength compared to the control plain concrete specimen. Single-hooked-end fibers with length and aspect ratios similar to fiber type A showed 13% to 30% increase in flexural strength at 1% dosage [15,16] which was lower than was observed for specimens with double-hooked-end fibers. It is worth mentioning that the results could have been influenced by specimen size variations. Among the 4D steel fibers, steel fiber type B (longer and thicker fiber) showed superior ultimate flexural strength than steel fiber type A (shorter and thinner fiber) at 1.0% fiber dosage. This effect might be attributed to the better distribution of the fiber and higher stiffness of anchorage of individual fibers due to the larger diameter. The advantage of steel fiber type C (greater anchorage and higher tensile strength) on ultimate flexural strength is reflected only at fiber contents of 0.5% and 0.75% (where the flexural strength results of FRCC are higher than FRCB). However, at 1% volume fraction, fiber types B and C showed similar effects. The increased anchorage advantage of fiber type C was not fully obtained at 1% fiber dosage because the concrete matrix fails before the fibers become fully effective. Therefore, to fully take advantage of fiber type C (at fiber dosage higher than 1%), the concrete strength needs to be increased.

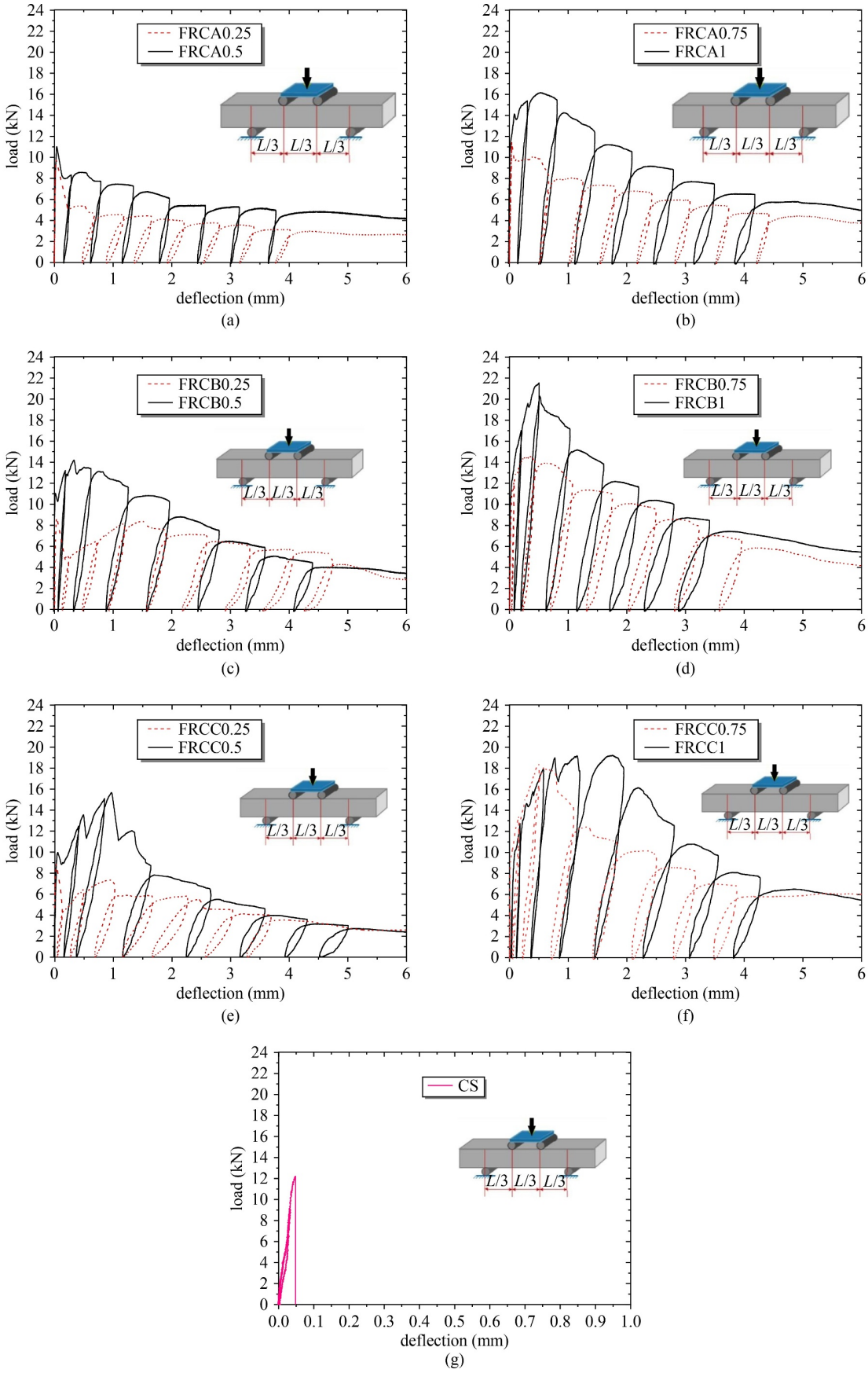

Fig. 6 Cyclic flexural load deflection plots for: (a) FRCA 0.25 and 0.5; (b) FRCA 0.75 and 1; (c) FRCB 0.25 and 0.5; (d) FRCB 0.75 and 1; (e) FRCC 0.25 and 0.5; (f) FRCC 0.75 and 1; (g) control specimen.

5.2.1 Fiber distribution

The performance of SFRC is controlled by the number of effective fibers oriented in the direction of the principal stress. The dissipated energy increases as more fibers cross the fractures. The fiber distribution in the flexural members was evaluated using an orientation factor, α, that was formulated by Krenchel [46] and further developed by Refs. [47,48]. The orientation factor was calculated by dividing the number of fibers in a specimen cross-section (N) to a theoretical number of fibers (N_{th}). N_{th} is based on the assumption that all the fibers are arranged perpendicular to the cross section. After the flexural test the prisms were broken into two halves at the fracture line, the number of fibers (N) was calculated by manually counting the fibers on the two sides, shown in Fig. 8(a). The orientation factor is calculated using Eq. (2). In Eq. (2), V_f is fiber volume fraction, A_f is cross-sectional area of a single fiber and A_c is cross-sectional area of the prism.

$$\alpha = \frac{N}{N_{th}} = N\frac{A_f}{V_f A_c}. \quad (2)$$

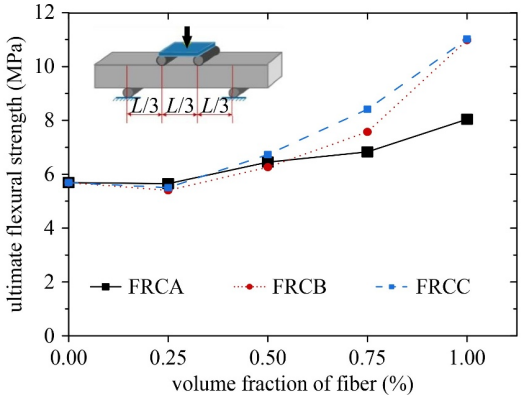

Fig. 7 Ultimate flexural strength versus fiber volume fraction of the three different types of fibers.

The fiber orientation factor results for all mixtures are presented on Fig. 8(b). All the mixtures showed a good orientation with fiber type A with a smaller α value than for types B and C. The range of α was 0.40 to 0.48 for fiber type A, 0.50 to 0.63 for fiber type B, and 0.53 to 0.61 for fiber type C. Dupont and Vandewalle [48] conducted a series of experiments to study distribution of fibers in a rectangular section for various dosage and dimension of hooked-end fibers using 150 mm × 150 mm cross-section beams. Evaluating their experimental results with Eq. (2), the average range of α for 35 and 40 mm long fibers at various proportions (0.45% to 0.75% volume fraction) provided 0.37 to 0.41. The average α value for 60 mm long fibers at different dosages varied from 0.4 to 0.83. Thus, although the current work used smaller size prisms, the orientation factor results were within the range observed for larger specimens from previous research [25,48]. Future research should consider larger size specimens.

5.2.2 Energy dissipation

The area under the hysteretic load-deflection curves represents the energy dissipated during the loading and unloading cycle [25]. Energy dissipation capacity is essential for structural performance under cyclic loads (e.g, earthquakes). Structures can survive seismic loads only if they can dissipate the energy exerted by the earthquake [28]. The cumulative energy dissipation versus displacement curves of all specimens, are plotted in Fig. 9. The cumulative energy dissipated by the specimens is calculated by summing up the area under the load-deflection curve before reaching the specified displacement. For all three steel fiber types, the cumulative dissipated energy considerably increased with the increase in fiber content. After reaching the peak stress, the energy dissipation is attained by the slip and straightening of the hooks in the fibers, and as the

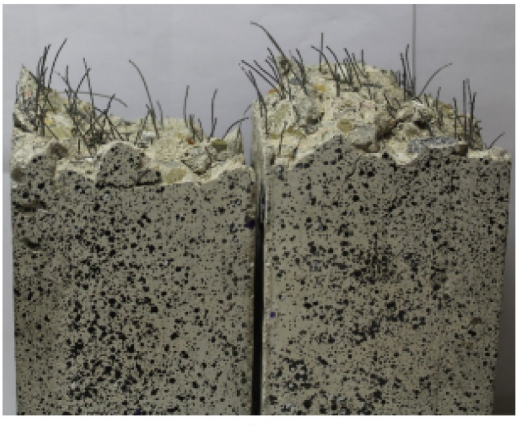

(a)

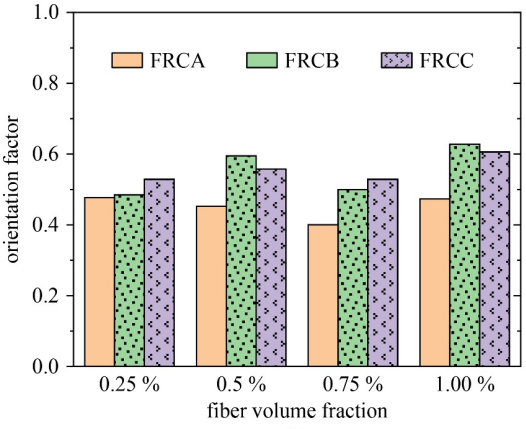

(b)

Fig. 8 (a) Fiber distribution in a fractured cross-section; (b) orientation factor for the three fiber types.

deflections increase, the fibers become more active and more energy is dissipated, as shown in Fig. 9.

Comparison of the amount of energy dissipation among the three different types of fibers is presented in Fig. 10. In all four percentages (0.25%, 0.5%, 0.75%, 1.00%) of fiber mixtures, fiber type A (shorter and smaller diameter) showed lower energy dissipation than fiber type B (longer and thicker), even though the two fibers have similar aspect ratios. The total energy dissipation at 4.0 mm mid-span deflection for FRCB1 is 39% higher than FRCA1. This higher energy dissipation characteristic of fiber type B compared to fiber type A might be due to its better distribution and higher mechanical anchorage from its longer end hook and higher stiffness due to larger diameter. Steel fiber type C has slightly higher energy dissipation than type B.

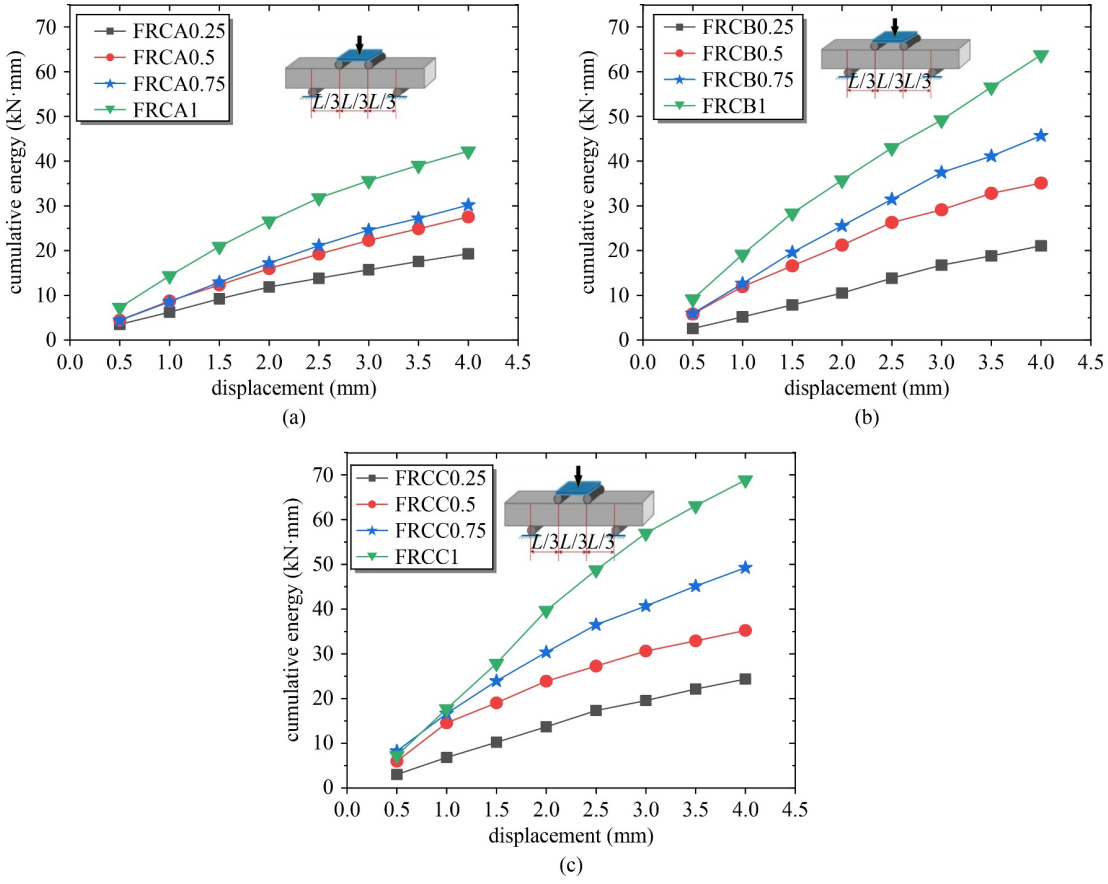

Fig. 9 Cumulative energy dissipation of specimens, the effect of fiber volume fraction for: (a) FRCA; (b) FRCB; (c) FRCC.

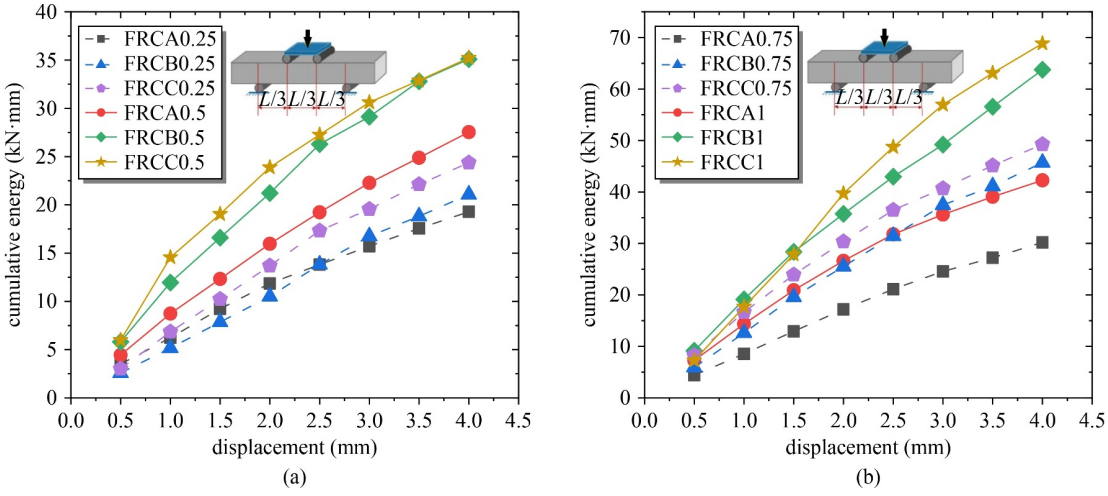

Fig. 10 Cumulative energy dissipation of specimens, the effect of fiber type for volume fractions: (a) 0.25% and 0.5%; (b) 0.75% and 1%.

5.2.3 Damage evolution

The addition of steel fibers in concrete enhances the damage tolerance of structures. The strengthening of the fibers during higher tensile stress leads to either the matrix damage in the fiber-matrix interface or the fiber damage [49]. Understanding the damage evolution plays a significant role to accurately predict the structural performance of SFRC [50]. The damage evolution for cyclic flexural behaviour of SFRC can be evaluated using stiffness degradation over subsequent cycles. The stiffness degradation was expressed in terms cyclic modulus (E_{cyc}) and the degree of reversibility (R) [25]. As shown in Fig. 11, the cyclic modulus is defined as the slope of a line connecting the start of unloading to beginning of reloading of the load deflection curve. The initial modulus (E_0) is the slope of the tangent line at beginning of the load deflection curve. The degree of reversibility is calculated as the ratio of the difference between maximum deflection and residual deflection to the maximum deflection, $R = (\delta_{max} - \delta_{residual})/\delta_{max}$.

5.2.3.1 Cyclic modulus

The cyclic modulus (E_{cyc}) decreases as the number of cycles and displacement decreases for all the fiber reinforced concrete studied, shown in Fig. 12. For most of the mixtures with similar fiber type early cycle modulus of elasticity is grater for higher percentage of fibers. For fiber type A, the 1% by volume of steel fiber has about twice initial stiffness than the 0.25% fiber dosage, shown in Fig. 12(a). While for steel fiber type B and C, mixture with the 1% steel fiber has about three times higher initial stiffness than the 0.25% fiber content, Figs. 12(b) and 12(c). And the difference in stiffness between various

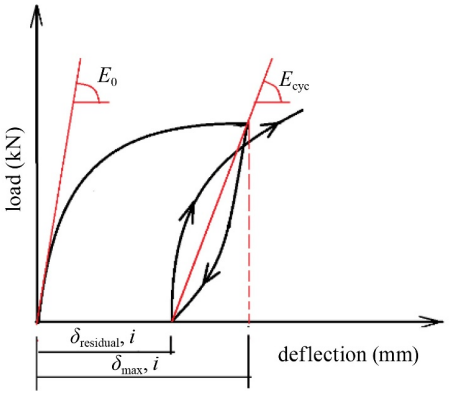

Fig. 11 Cyclic damage parameters.

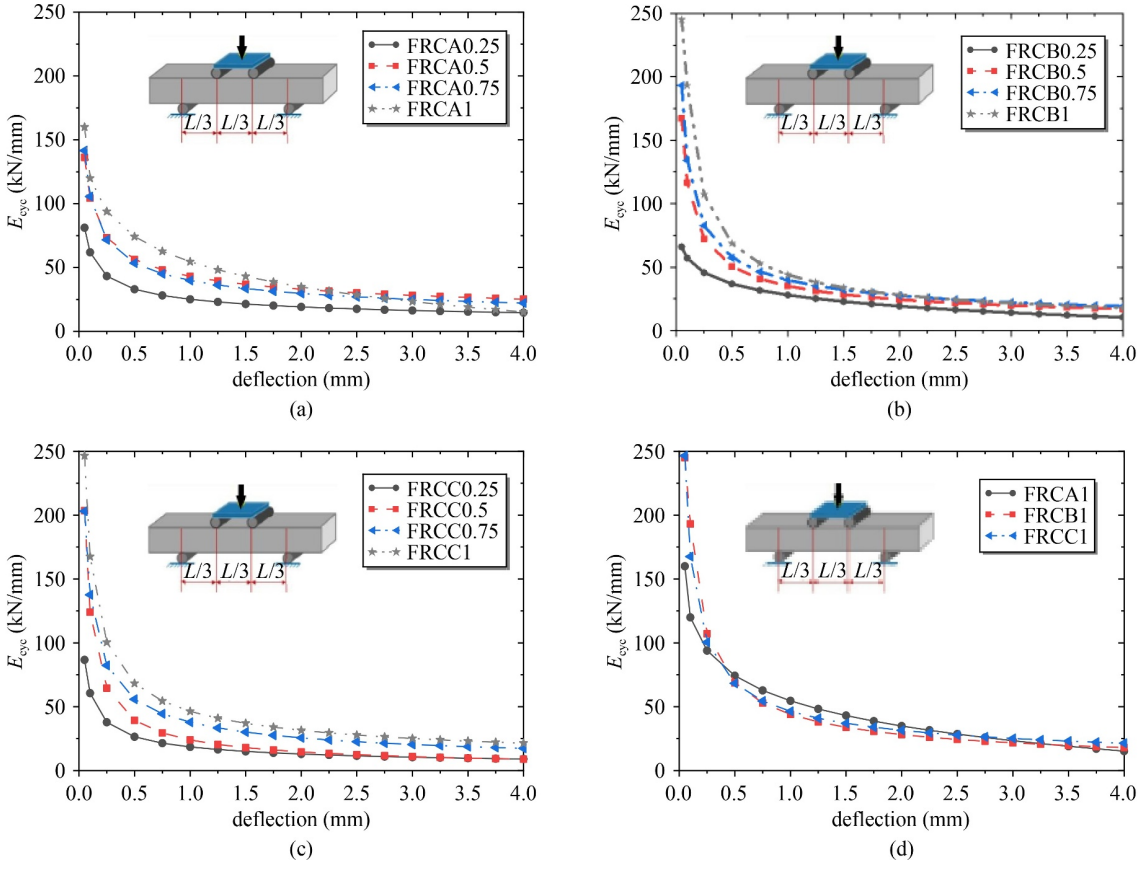

Fig. 12 Cyclic modulus of elasticity for: (a) FRCA; (b) FRCB; (c) FRCC at different fiber percentage; (d) the three fiber types at 1% fiber content.

fiber dosages decreases as the number of cycles grows as the contribution of the fibers lowers by pulling of the fibers by the widening of cracks. Mixture with 1% of the 30 mm long fiber (FRCA1) has 35% less initial stiffness than the similar dosage 60 mm long fibers (FRCB1 & FRCC1) and the difference in decreases after a deflection of 0.25 mm, shown in Fig. 12(d).

5.2.3.2 Degree of reversibility

Figure 13 presents plots of degree of reversibility versus deflection across cycles. As expected, the degree of reversibility decreases with the increase in number of cycles caused by the material progressive damage. For all the fiber types, the degree of reversibility is higher for 1% fiber content. During the initial cycles, the reversibility is higher due to the elastic deformation of the fibers during loading and the recovery while unloading. On the subsequent cycles, the reversibility decreases as the anchors straighten and/or break leading to irreversible deformation. The grater fiber dosage in the mixture produced a higher reversibility due. It was also observed that higher anchorage and larger fiber size increased the degree of reversibility. At 1% fiber dosage, fiber type C (higher anchorage and 60 mm long) showed greater reversibility than fiber types B and C as shown in Fig. 13(d).

5.2.4 Crack evolution from digital image correlation

DIC technique can be considered as a useful method to evaluate crack propagation. Figure 14 shows the deflection measurements of one of the specimens relative to the center of the specimen using DIC and LP during initial cycles. DIC and LP measurements are in good agreement (Fig. 14); which shows the DIC method used in this study is valid to measure the displacements.

Figure 15 shows the longitudinal strain contours for the SFRC prisms after unloading at the 3rd, 6th and 9th cycles. The contours show that for all the three fiber types as the percentage of steel fiber in the mixture increases the cracks change from single major to multiple smaller size cracks. The formation of these multiple cracks is responsible for the higher energy dissipation in prisms with more percentage of steel fiber. After unloading at the third cycle, the longitudinal strains for steel fiber type B and C are lower than the strains in mixtures with steel fiber type A. In addition, FRCB and FRCC mixtures with more than 0.5% steel fiber show multiple smaller cracks, while FRCA with more than 0.5% steel fiber show fewer major cracks. This shows that the fiber types B and C perform better in delaying crack propagation and re-centering compared to the fiber type A.

Cumulative crack width at the bottom of the specimens

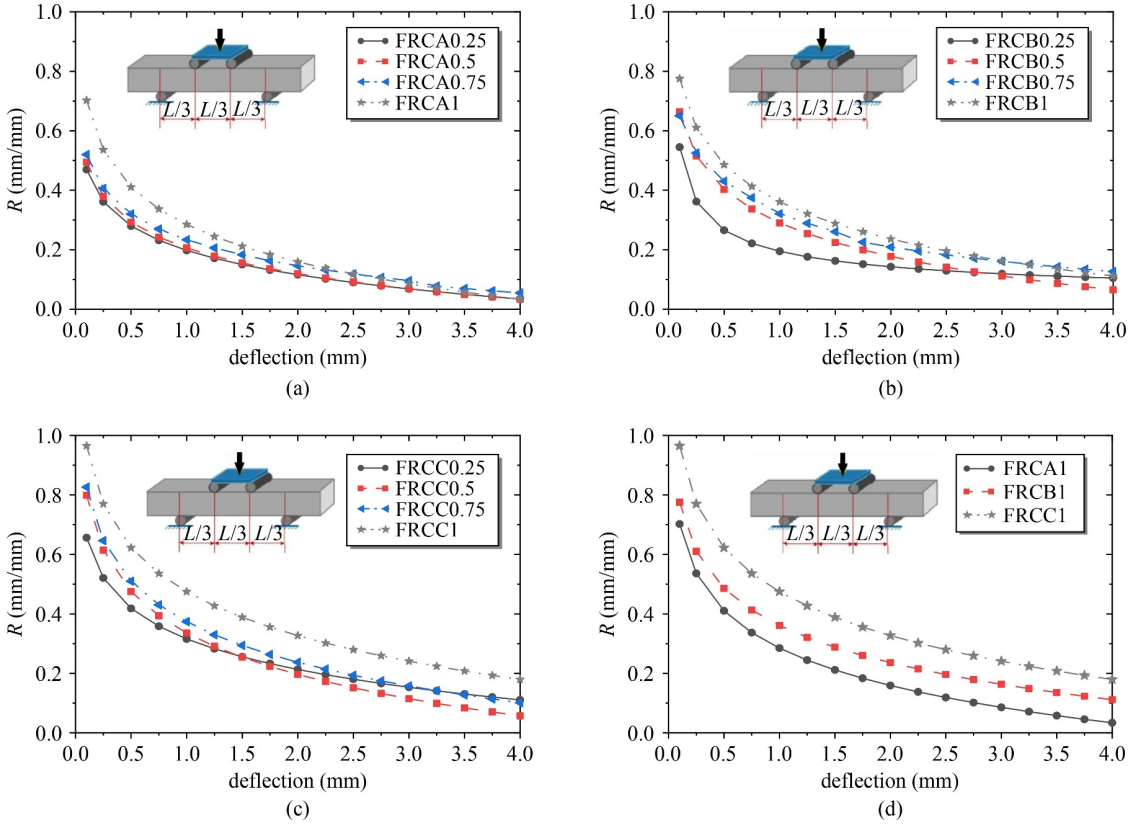

Fig. 13 Degree of reversibility across cycles for: (a) FRCA; (b) FRCB; (c) FRCC at different fiber percentage; (d) the three fiber types at 1% fiber content.

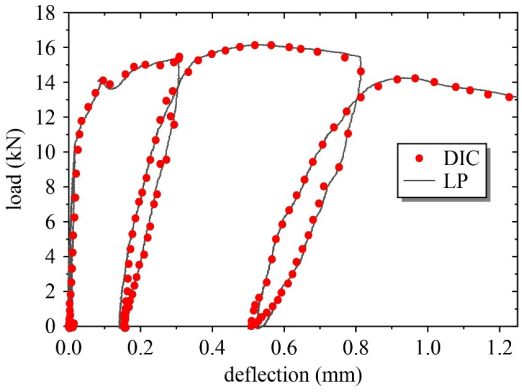

Fig. 14 Comparison between LP reading and DIC measurement for load deflection plot of FRCA1 during initial cycles.

is measured using DIC and the crack width evolution over the cycles is presented in Fig. 16. For all three fiber types, the increase in volume of fraction of fibers limited the width of cracks and increased the re-centring (crack width reduction after unloading to a given cycle). The cumulative crack width for the different steel fiber types at equal fiber content is similar except the FRCC1 which has higher re-centring and lower crack width than the other specimens with similar fiber dosage (Fig. 16(d)). It would be worth noting that although the cumulative crack width for FRC with fiber A and fiber B is similar, mixtures with fiber A had fewer and wider cracks, while FRC with fiber B had multiple narrow cracks. This made FRCB mixtures to dissipate considerably larger energy than FRCA.

6 Finite element modeling

3D nonlinear finite element modeling is used to simulate the flexural load deflection and crack formation response of the fiber reinforced concrete prisms. The FEM was conducted using the concrete damaged plasticity (CDP) model in ABAQUS [51]. The material parameters, the modeling technique and the results are presented in this section. The section presents the numerical results only for the FRCC1 (fiber reinforced concrete with 1% fiber type C volume fraction).

6.1 Concrete damaged plasticity model

CDP model has the potential to represent the full inelastic responses of concrete both in tension and compression, that makes it a great selection for modeling the structural response of both plain concrete and fiber reinforced concrete structures under monotonic and cyclic loading [52,53]. In addition to the compressive and tensile stress strain relationships of the fiber reinforced concrete, the CDP model requires other additional input material parameters which are discussed in the next sections. The complete compressive stress strain relationship for the fiber reinforced concrete was adopted from the cylindrical compressive strength tests presented in the section 5.1.2

6.2 Tensile behaviour of fiber reinforced concrete

The tensile strength is one of the most essential properties of the fiber reinforced concrete and can be characterized by a stress crack width relationship. Direct tensile tests might be the best way to determine the tensile behaviour of fiber reinforced concrete since directly provides us with the stress strain behaviour. However, direct tensile tests are difficult to perform because they require specialized equipment and the results are sensitive to stress concentration, shape, boundary conditions, and specimen size compared to gravel and fiber size [54,55]. Although splitting tensile test is a cheap and simple way to determine tensile behaviour of FRC, stress localization at load application points might lead to overestimating the SFRC strength [56]. Simplified inverse analysis from four-point bending tests of unnotched prisms is one of the easiest and appropriate methods to determine the tensile stress−strain and stress-crack opening relationships of FRC [57]. It is well established that increasing the volume fraction and mechanical anchorage of fibers increases the tensile stress of SFRC [15,20,22]. The multilinear tensile stress-crack width relationship (σ−w) of single-hooked-end (3D), and double-hooked-end (4D and 5D) SFRC was investigated by Gao et al. [58]. The results showed that, with increasing fiber dosage, the σ−w relationship changed from tensile strain softening to strain hardening. SFRC with 4D and 5D fibers showed tensile stress hardening at 1.5% and 1% fiber volume fractions, respectively. Similarly, self-compacting SFRC with 0.5% and 1% volume 5D steel fibers exhibited tensile strain hardening that was due to the high anchorage and high strength property of 5D fibers [22]. Thus, the FRCC1 (fiber reinforced concrete with 1% 5D fiber) modeled in this section was considered as a tension strain hardening material. Constitutive law in the present work is determined using the inverse analysis method from four point bending tests provided by the Canadian highway bridge design code, CSA S6:19 Annex A8.1 [36]. A specimen size of 76 mm × 76 mm × 292 mm (similar to the prisms for cyclic loading) under four-point bending at a constant rate of 0.6 mm/min was used. Figure 17 shows the relationship parameters from the load deflection plots. It is worth mentioning that this method applies for tension hardening FRC and used only for FRCC1 among the mixtures considered in this paper. The mixtures other than FRCC1 should be modeled as tension softening FRC, which is not covered in this work. The parameters determined from the slope deflection

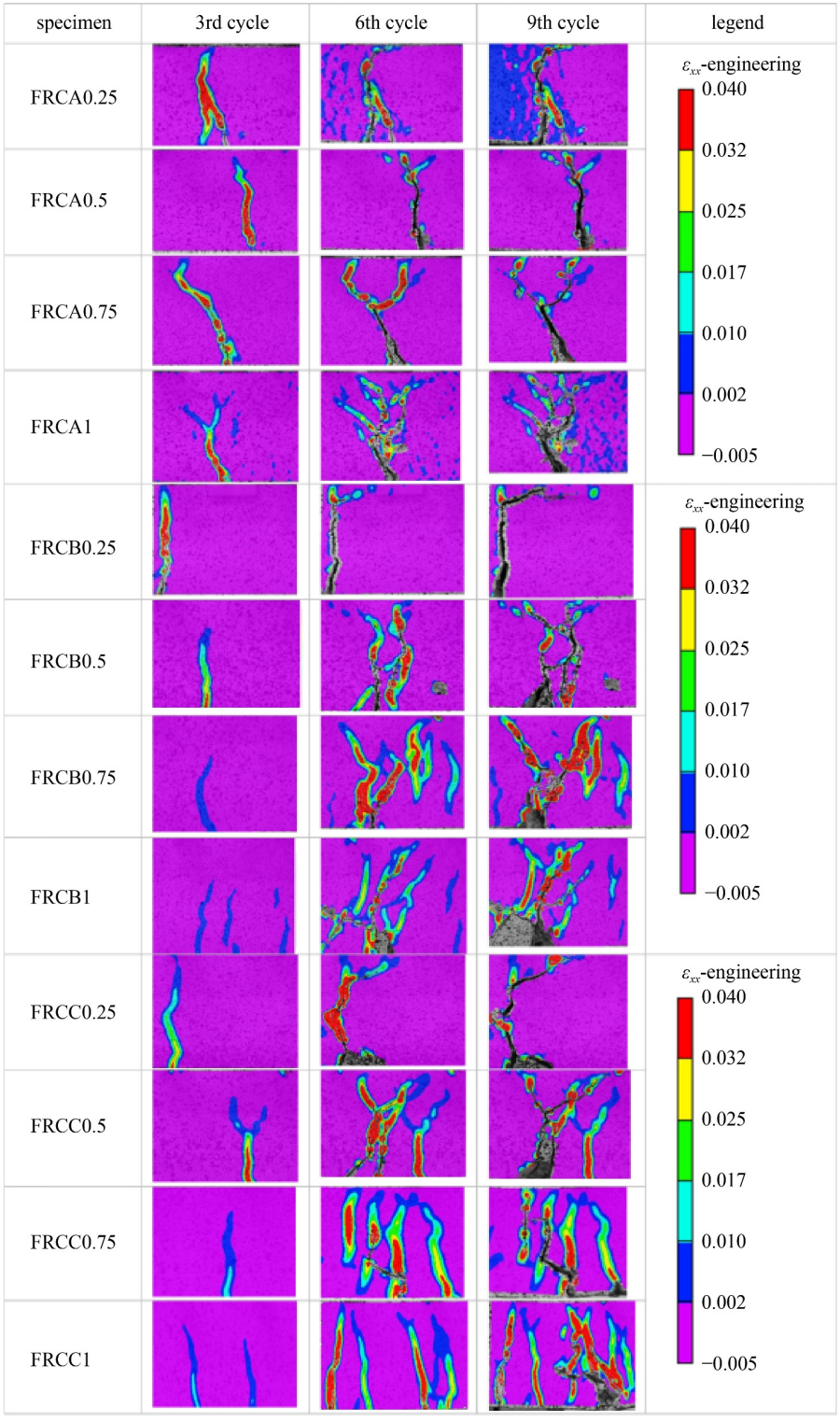

Fig. 15 Longitudinal strain field (ε_{xx}) as measured by DIC after unloading for 3rd, 6th and 9th cycles.

curve include: the initial slope s_0; points 1 and 2 that represent the intersection of slope deflection curve and the straight line starting at the origin with slope of 75% and 40% of the initial slope s_0; and points 3 that represent 97% maximum applied load and point 4 that denote 80% of the load at point 3. Then Eqs. (3)–(9) were used to determine the post cracking tensile properties of FRC for a prism size of width (b), depth (h) and distance (l) between supports. Then modulus of elasticity in tension (E_{t0}), the cracking strength (f_{crm}), ultimate tensile strength (f_{FU}), cracking strain (ε_{cr}), strain corresponding to ultimate strength (ε_{tu}) and the crack opening displacement

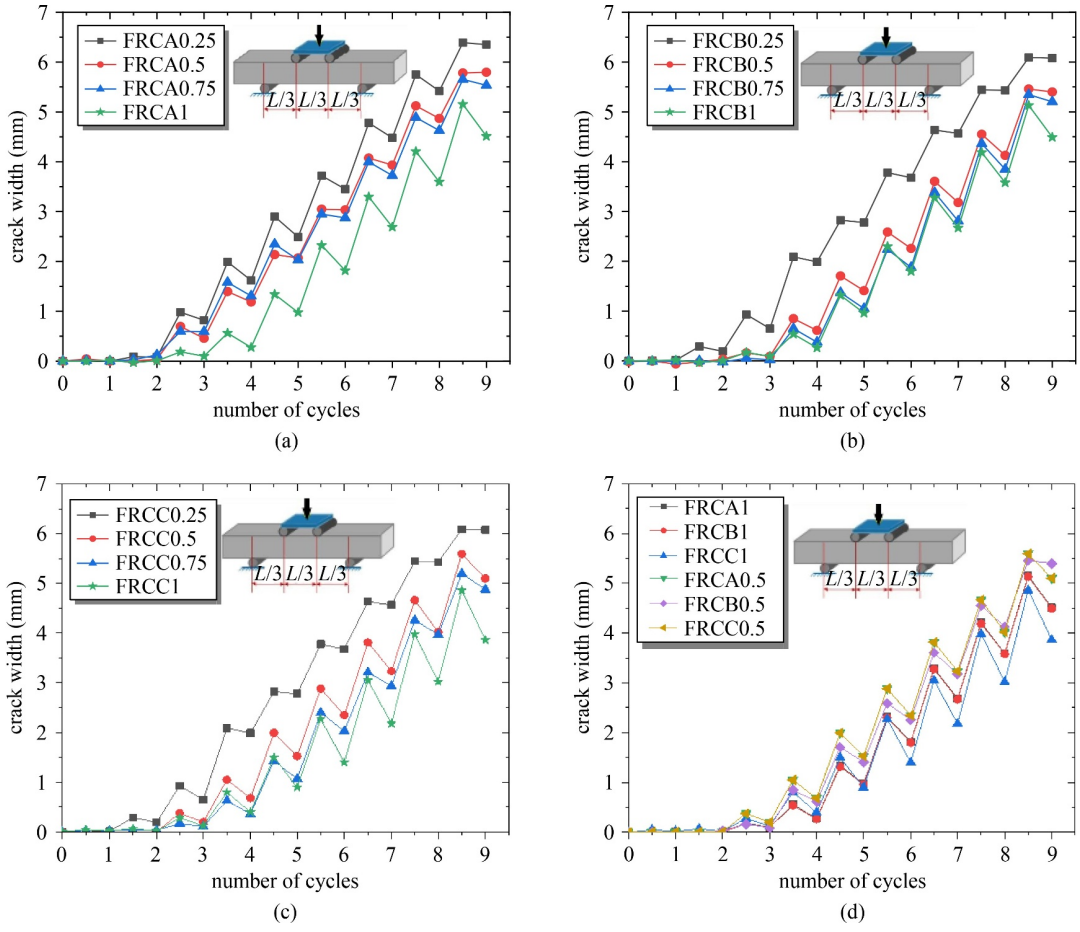

Fig. 16 Longitudinal crack width evolution at the bottom of specimens measured using DIC for: (a) FRCA; (b) FRCB; (c) FRCC for different fiber volume fraction; (d) between the three fiber types at 0.5% and 1% fiber dosage.

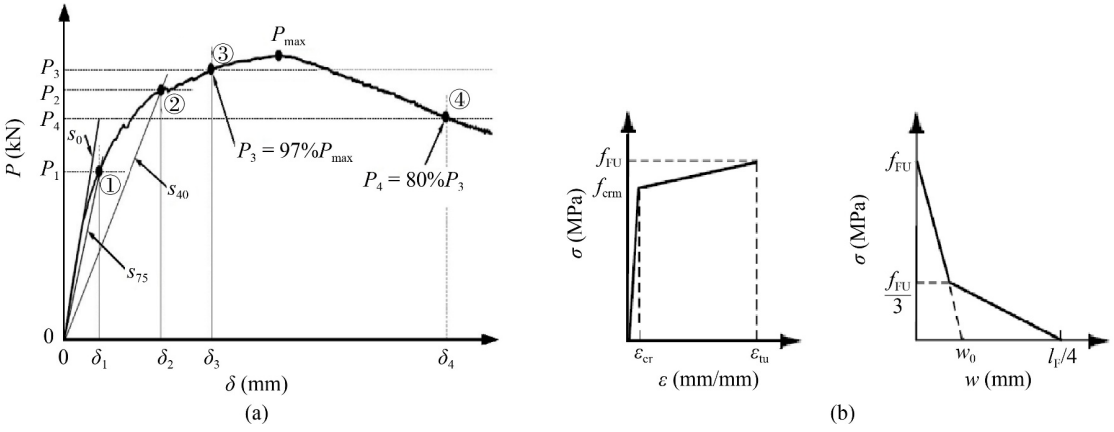

Fig. 17 (a) Key points from the load deflection curve used for inverse analysis; (b) the bilinear tensile behaviour found using the inverse analysis.

were calculated using those equations. Equations (3)–(9) are valid only for tension hardening FRC specimens with unsupported length (l) to depth (h) ratio equal to 3 [36].

$$E_{t0} = \frac{7.2}{b} s_0, \tag{3}$$

$$f_{crm} = k_1 \frac{P_1 l}{bh^2}, \text{ where } k_1 = \frac{(p_1/p_2)^{0.19}}{1.63}, \tag{4}$$

$$\varepsilon_{cr} = \frac{f_{cm}}{E_{f0}}, \tag{5}$$

$$\varepsilon_{tu} = k_2 \varepsilon_{cr}, \text{ where } k_2 = \left(7.65 \frac{\delta_3}{\delta_1} - 10.53\right), \tag{6}$$

$$f_{FU} = k_3 f_{cm}, \text{ where } k_3 = k_2^{-0.18} \left(2.46 \frac{p_3}{p_1} - 1.76\right), \tag{7}$$

$$\varepsilon_{t0} = k_4 \varepsilon_\sigma, \text{ where } k_4 = k_3^{-0.37} k_2^{0.88} \left(3\frac{\delta_4}{\delta_3} - 1.80\right), \quad (8)$$

$$w_0 = \left(\varepsilon_{t0} - \varepsilon_{tu} + \frac{10 f_{FU}}{3E_{t0}}\right)\frac{3h}{2}. \quad (9)$$

Figure 18 presents tensile properties of FRCC1 calculated from the inverse analysis. The ultimate tensile strength (f_{FU}) results for FRCC1 from splitting tensile strength tests are twice those of the results from the inverse analysis. This effect might attributed to the over estimating tendency of splitting tensile tests due to stress localization around load application points [56].

6.3 Finite element analysis

The tensile stress−strain and stress-crack width results (shown in Fig. 18) were used as an input tensile property in the FEA analysis. Figure 19 shows the geometry of the fiber reinforced concrete prisms. Symmetry along *XY* plane was used and half of the specimen is modeled. In addition to the FRC specimen the test setup including the support and loading steel rollers were included in the FEA model, this will help to represent the localized deformation due to the rotations of the steel shafts [59,60]. The friction coefficient between the FRC and the steel shafts was equal to 0.35 and between the steel plate and steel shafts was takes as 0.25. The support conditions represent the experimental setup with a displacement loading applied at the top steel bars. Support was provided by the combination of the bottom steel bars and plates. The FRC prism was modeled using eight node hexahedral elements with reduced integration (C3D8R).

The material properties and plasticity parameters of CDP model for the fiber reinforced concrete (FRCC1) are shown in Table 5. The compressive strength is determined from the experimental results as presented in Subsubsection 5.1.1. Stress−strain relationship in tension is determined using the simplified inverse analysis, discussed in Subsection 6.3. Modulus of elasticity shown in Table 5 is the average of the elastic modulus in compression (E_c) and tensile modulus of elasticity (E_{t0}). E_c was determined from the compressive stress-strain relationship according to ASTM C469/C469M-14 [39], defined as the slope of the line connecting 0% to 40% of maximum compressive stress, discussed in Section 5.1.2. While E_{t0} is calculated from Eq. (2). Poisson's ratio was taken as 0.2 and mass density of the FRC was calculated to be 2480 kg/m^3.

The plasticity parameters for CDP include dilation angle, eccentricity, stress ratio, shape factor, and viscosity. Dilation angle (ψ) of concrete defines the change in volume associated to shear deformation. The effects of variation in dilation angle values were evaluated with values of 25°, 30° and 35°. The default value for the eccentricity is 0.1 which assumes the concrete has similar dilation angle regardless of the variation in confining pressures [51]. Similarly, the default of 1.16 was taken for the ratio of the biaxial compressive strength to the uniaxial compressive strength (σ_{b0}/σ_{c0}). The shape factor (k_c) determines the shape of the of the yield surface in the deviatory plane with a default value of 0.667 [51].

Material damage at the softening stages in CDP was expressed in terms of compression damage parameter (d_c) and tensile damage parameter (d_t). The compression damage parameter is calculated from the compression plastic strain (ε_c^{pl}) and inelastic strains (ε_c^{in}) using Eq. (10). The inelastic strain (ε_c^{in}) for a given compressive stress (σ_c) is the difference between the total strain (ε_c), and the elastic strain (ε_{0c}^{el}), where $\varepsilon_{0c}^{el} = \sigma_c / E_{c0}$.

$$\varepsilon_c^{pl} = \varepsilon_c^{in} - \frac{d_c}{1-d_c}\frac{\sigma_c}{E_{c0}}, \quad (10)$$

$$\varepsilon_c^{pl} = \varepsilon_c - \varepsilon_{0c}^{el}. \quad (11)$$

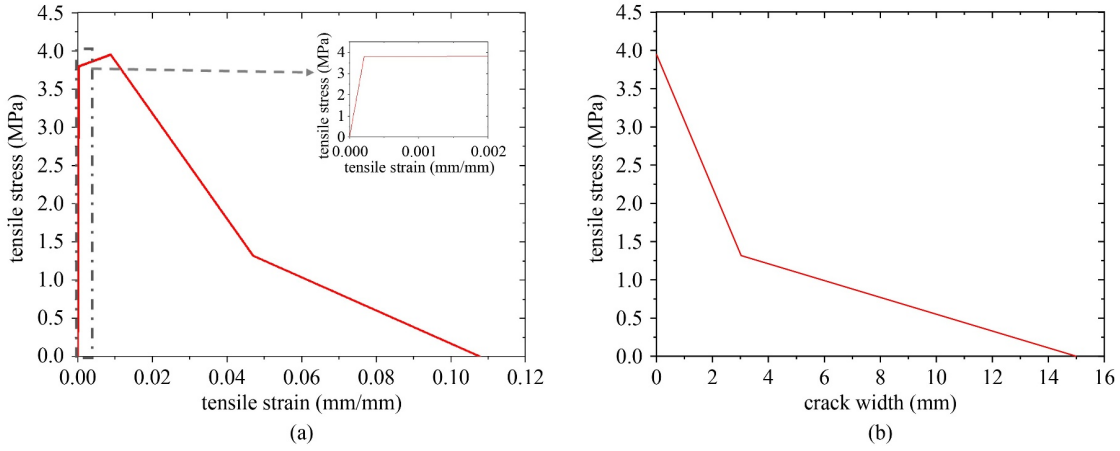

Fig. 18 Tensile properties of FRCC1 calculated from inverse analysis: (a) stress−strain properties; (b) stress-crack width properties.

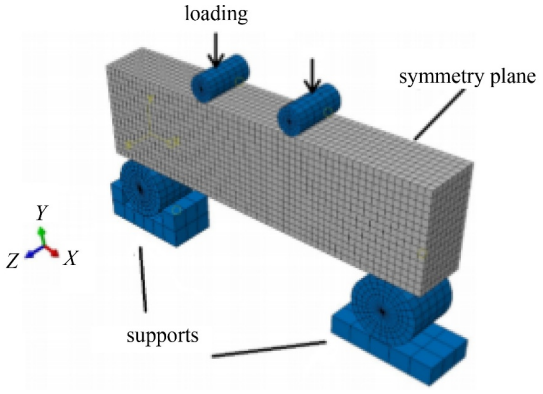

Fig. 19 Symmetrical model of FRC prism.

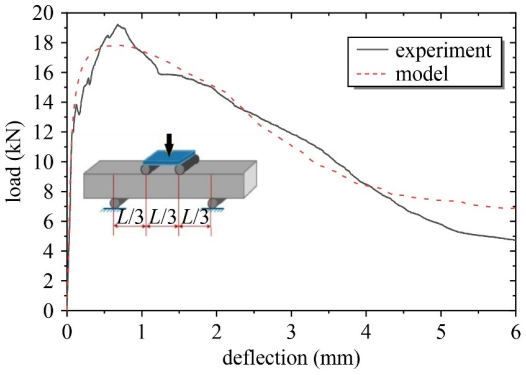

Fig. 20 Comparison between FEA and test in terms of load deflection response.

Table 5 Material property and plasticity parameters for concrete damage plasticity model of FRCC1

parameter	value
compressive strength, f_c' (MPa)	48.9
tensile strength, f_{FU} (MPa)	3.95
modulus of elasticity, E_c (GPa)	20.45
dilation angle, ψ (°)	30
eccentricity	0.1
stress ratio, σ_{b0}/σ_{c0}	1.16
shape factor, k_c	0.667
viscosity parameter	0

The tensile damage parameter (d_t) is calculated from Eq. (12). In these equations ε_t^{pl} is the tensile plastic strain and ε_t^{ck} is the cracking strain corresponding to a tensile stress (σ_t). The cracking strain is calculated using Eq. (13), where ε_t and ε_{0t}^{el} denote the total and elastic tensile strain, respectively, and $\varepsilon_{0t}^{el} = \sigma_t / E_{t0}$.

$$\varepsilon_t^{pl} = \varepsilon_t^{ck} - \frac{d_t}{1-d_t}\frac{\sigma_t}{E_{t0}}, \tag{12}$$

$$\varepsilon_t^{ck} = \varepsilon_t - \varepsilon_{0t}^{el}. \tag{13}$$

6.4 Finite element analysis results

The finite element analysis (FEA) results for the four-point bending test under monotonic and cyclic loading of double-hooked-end fiber reinforced concrete at the 1% fiber content of fiber type C (FRCC1) are presented in this section. The load deflection responses of the experiment and the FEA model are shown in Fig. 20. Based on the proper calibration that has been conducted for the selection of the material parameters, the FEA results seem to be in agreement with the experimental results and this indicates the predictive capability of the FEA model to analyse SFRC.

The concrete damage plasticity model assumes initiation of crack when the maximum principal stress becomes positive. These cracks happen perpendicular to the maximum principal stress and the crack pattern is described using the principal stress distribution [61]. Crack patterns at 2 mm deflection for the experimental specimen and the model are shown in Fig. 21. Cracks form at the bottom tensile face and propagate towards the compression face (Fig. 21(a)). Similar cracking is shown in the FEA model in Fig. 21(b).

Finally, the calibrated model is used to simulate the cyclic flexural response of FRCC1 for the loading protocol discussed in Subsection 4.1. Comparison between the experimental specimen and the model are presented in Fig. 22. The model reasonably predicted the experimental results for most of the cycles. However, there is a considerable difference between the FEM and the experiment on the slope of the unloading path at the later cycles. The test specimen has a lower unloading slope that led to a reversibility (R). This shortcoming could be attributed to the limitations of the CDP model to account for the degradation in cyclic modulus of elasticity across repeated cycles even if damage parameters were considered in both tension and compression.

Comparison of the longitudinal strain between DIC and FEA after unloading to the third, sixth and ninth cycles is shown in Fig. 23. The FEA model showed lower strain at the initial cycles and higher strains during the later cycles than the results from DIC. This difference could be a result of limitation on the tensile stress strain constitutive law obtained by inverse analysis and the variation between model and experimental setup details like restraint provided by steel rolls. At the end of the third cycle, the test specimen reached had an ultimate strain of 0.017 while the maximum strain in the FEA model was 0.010. At the end of the 6th cycle the DIC and FEA showed an ultimate strain of 0.040 and 0.045, respectively. At the end of the 9th cycle the DIC readings for some of the section with maximum strain was not recorded due to the loosening of reference dots at the

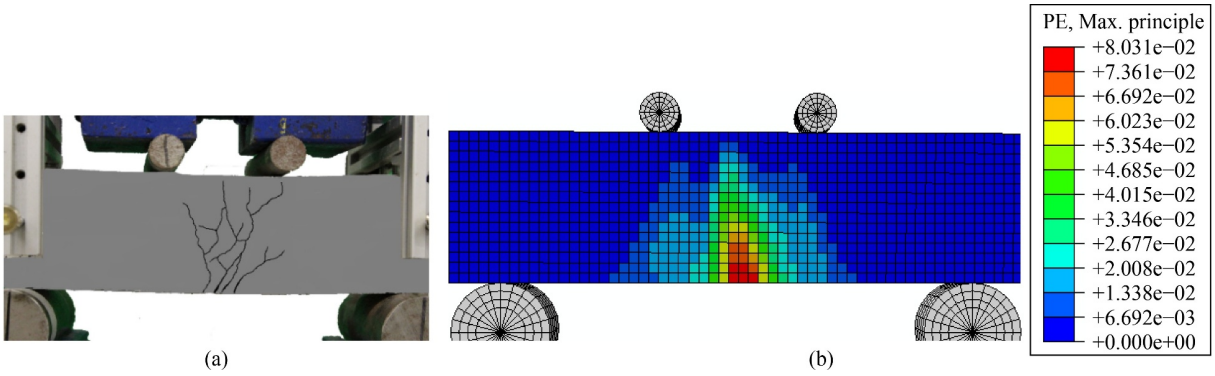

Fig. 21 Crack pattern at 2 mm deflection: (a) experiment; (b) FEA model.

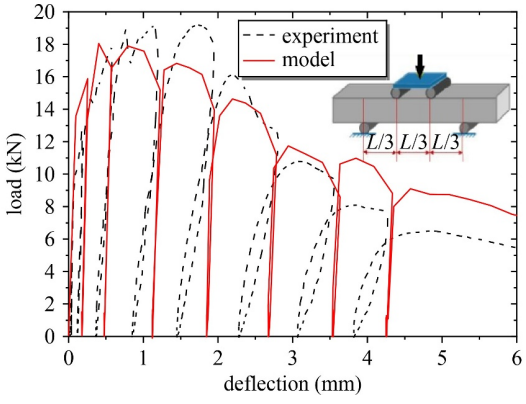

Fig. 22 Load deflection response of FRCC1 model and experiment.

location of bigger cracks, while a maximum strain of 0.15 was recorded in the FEA as shown in Fig. 23.

7 Conclusions

The mechanical properties and the cyclic flexural performance of SFRC with three different double-hooked-end steel fibers were experimentally studied. The experimental results considered DIC to obtain the developed strains and cracking, while an advanced nonlinear FEA model was calibrated to understand better the behavior of SFRC. The following conclusions can be drawn.

1) The addition of double-hooked-end steel fibers improved the 28 d age tensile strength, strain at ultimate compressive load and post ultimate load strain, and the 90 d age compressive strength, while slightly reduced the 28th day compressive strength in some specimens.

2) Among the two 4D fibers, steel fiber type B (the longer and thicker fiber) was found to be superior in tensile strength, ultimate flexural strength, and in energy dissipation for fiber dosages greater than 0.5% by volume.

3) The comparison between the present experimental results with previously developed models for the mechanical properties of SFRC show that the models do not accurately predict all the mechanical properties of the specimens and thus a more comprehensive model is needed for wider application of double-hooked-end SFRC.

4) Double-hooked-end steel fibers enhanced both the ductility and the ultimate flexural strength of the prisms under cyclic loading. The improvement in flexural strength increased with the increase in the volume fraction of steel fibers. The ultimate flexural strengths of specimens with 1% steel fiber for the three fibers namely: FRCA1, FRCB1, and FRCC1 were 41%, 92%, and 94%

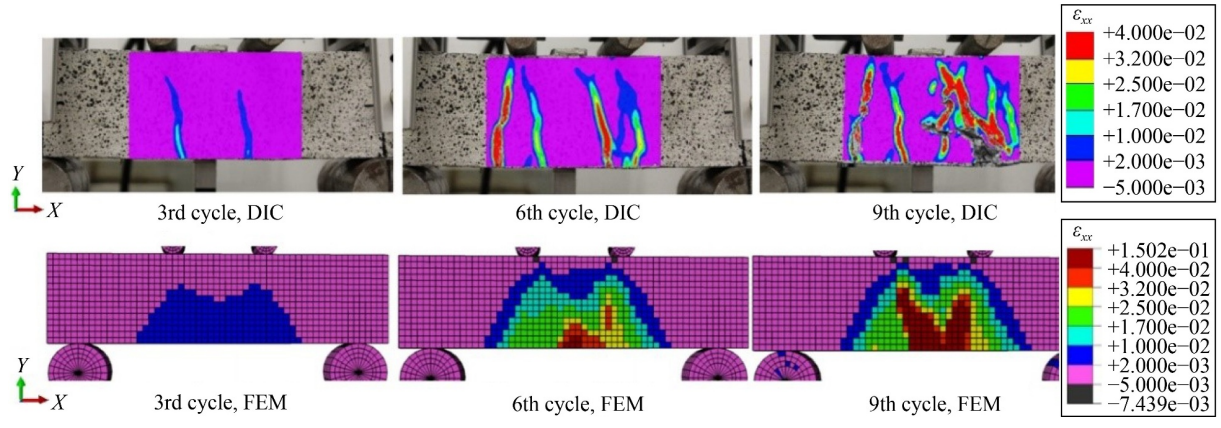

Fig. 23 Longitudinal strain distribution results from DIC and FEA.

higher than the control plain concrete specimen, respectively.

5) The cumulative energy dissipation and degree of reversibility under cyclic loading was significantly increased with the addition of fiber for all three fiber types.

6) Among the two 4D steel fibers, fiber type B (longer and thicker fiber) had superior flexural strength and energy dissipation characteristics than did steel fiber type A (shorter and thinner fiber). SFRC with steel fiber type C (5D) showed better flexural strength and energy dissipation than fiber type B at dosages less than 1% by volume fraction. For 1% steel fiber dosage, fiber type C and type B have similar responses to each other, and to take advantage of the strength and anchorage of steel fiber type C (at a higher volume fraction of fibers) the compressive strength of the matrix needs to be increased.

7) DIC analysis provides an accurate visualization of the evolution and width of cracks during cyclic flexural loading. Mixtures with a higher dosage of steel fiber show multiple smaller cracks, while mixtures with smaller fiber content have fewer wider cracks. Fiber type C showed better crack closing capacity than fiber type A and fiber type B.

8) The presented 3D FEA model showed comparable results with the experiments in terms of monotonic and cyclic load deflection response and crack distribution. The strain distribution results from the FEA produced comparable strain distribution and ultimate strain with the results from the DIC.

Acknowlegdements The authors would like to thank the MasterCard Foundation Scholars Program for the financial support provided to the first author.

Appendix

Table A1 presents previously published model predictions for 28 d age SFRC in compression and tension that are used in Subsubsection 5.1.3 (Fig. 5). In these equations σ and ε represent any point on the stress strain

Table A1 Models for strength properties predictions of SFRC

reference	model
Thomas and Ramaswamy [16]	$f'_{cf} = f'_c + 0.05476 f'_c RI_v + 1.02 RI_v$ (MPa) $f_{tf} = 0.6874(f'_c)^{0.5} + 0.3142(f'_c)^{0.5} RI_v + 0.052 RI$ (MPa) f_{tf} = splitting tensile strength $E_{cf} = 4.997(f'_c)^{0.5} + 0.5 f'_c RI_v + 0.39 RI$ (GPa) $\varepsilon_{cof} = \left[528.513(f'_c)^{0.3943} + 4.2605 f'_c RI_v + 484.95 RI_v\right] \times 10^6$ $E_c = 4.2\sqrt{f'_c}$ (GPa) for 30 MPa $\leqslant f'_c \leqslant$ 75 MPa $RI_v = V_f L_f / D_f$, V_f = volume fraction of steel fiber
Nataraja et al. [44]	$\dfrac{\sigma}{f'_{cf}} = \dfrac{\beta\left(\dfrac{\varepsilon}{\varepsilon_{cof}}\right)}{\beta - 1 + \left(\dfrac{\varepsilon}{\varepsilon_{cof}}\right)^{\beta}}$ $f'_{cf} = f'_c + 2.1604(RI_w)$ $\varepsilon_{cof} = \varepsilon_{co} + 446 \times 10^{-6}(RI_w)$ $\beta = 1.093 + 0.7132(RI_w)^{-0.926}$ for hooked-end fibers $RI_w = W_f L_f / D_f$, W_f = Weight fraction of steel fiber σ and ε denote points on the stress strain relation graph without specific experimental data $\varepsilon_{co} = 0.002$
Ou et al. [45]	$\dfrac{\sigma}{f'_{cf}} = \dfrac{\beta\left(\dfrac{\varepsilon}{\varepsilon_{cof}}\right)}{\beta - 1 + \left(\dfrac{\varepsilon}{\varepsilon_{cof}}\right)^{\beta}}$ $f'_{cf} = f'_c + 2.35(RI_v)$ (MPa) $\varepsilon_{cof} = \varepsilon_{co} + 0.0007(RI_v)$ $\beta = 0.71(RI_v)^2 - 2.0(RI_v) + 3.05$ $RI_v = V_f L_f / D_f$, V_f = volume fraction of steel fiber
Lee et al. [43]	$\varepsilon_{of} = (-0.0003 RI_v + 0.0018)\left(f'_{cf}\right)^{0.12}$ $E_{cf} = (-367 RI_v + 5520)(f'_{cf})^{0.41}$ (MPa) $\sigma = f'_{cf}\left[\dfrac{A\left(\dfrac{\varepsilon}{\varepsilon_{cof}}\right)}{A - 1 + \left(\dfrac{\varepsilon}{\varepsilon_{cof}}\right)^{B}}\right]$ for $\varepsilon_c/\varepsilon_o \leqslant 1.0$, $A = B = \left[\dfrac{1}{1 - \left(\dfrac{f'_{cf}}{\varepsilon_{cof} E_{cf}}\right)}\right]$ for $\varepsilon_{cf}/\varepsilon_{cof} \leqslant 1.0$ $A = 1 + 0.723[RI_v]^{-0.957}$ for $\varepsilon_{cf}/\varepsilon_{cof} > 1.0$ $B = \left(\dfrac{f'_{cf}}{50}\right)^{0.064}\left[1 + 0.882(RI_v)^{-0.882}\right] \geqslant A$ for $\varepsilon_{cf}/\varepsilon_{cof} > 1.0$ $RI_v = V_f L_f / D_f$, V_f = volume fraction of steel fiber

curves while f'_c, ε_{co}, f'_{cf}, and ε_{cof} denote the plain concrete peak compressive stress, plain concrete strain at peak compressive stress, SFRC peak compressive stress and SFRC strain at peak compressive stress, respectively.

References

1. di Prisco M, Plizzari G, Vandewalle L. Fibre reinforced concrete: New design perspectives. Materials and Structures, 2009, 42(9): 1261−1281
2. ACI 544.9R-17: Report on Design and Construction of Steel Fiber-Reinforced Concrete Elevated Slabs. Farmington Hills: American Concrete Institute, 2017
3. Soutsos M, Le T, Lampropoulos A. Flexural performance of fibre reinforced concrete made with steel and synthetic fibres. Construction & Building Materials, 2012, 36: 704−710
4. Mohammadi Y, Singh S, Kaushik S. Properties of steel fibrous concrete containing mixed fibres in fresh and hardened state. Construction & Building Materials, 2008, 22(5): 956−965
5. Chanthabouala K, Teng S, Chandra J, Tan K H, Ostertag C P. Punching tests of double-hooked-end fiber reinforced concrete slabs. ACI Structural Journal, 2018, 115(6): 1777−1789
6. Sutton M A, Orteu J J, Schreier H. Image correlation for shape, motion and deformation measurements: Basic concepts, theory and applications. Springer Science & Business Media, 2009
7. Alam S Y, Saliba J, Loukili A. Fracture examination in concrete through combined digital image correlation and acoustic emission techniques. Construction & Building Materials, 2014, 69: 232−242
8. Aggelis D, Verbruggen S, Tsangouri E, Tysmans T, Van Hemelrijck D. Characterization of mechanical performance of concrete beams with external reinforcement by acoustic emission and digital image correlation. Construction & Building Materials, 2013, 47: 1037−1045
9. Mahal M, Blanksvärd T, Täljsten B, Sas G. Using digital image correlation to evaluate fatigue behavior of strengthened reinforced concrete beams. Engineering Structures, 2015, 105: 277−288
10. Gencturk B, Hossain K, Kapadia A, Labib E, Mo Y L. Use of digital image correlation technique in full-scale testing of prestressed concrete structures. Measurement, 2014, 47: 505−515
11. Boulekbache B, Hamrat M, Chemrouk M, Amziane S. Failure mechanism of fibre reinforced concrete under splitting test using digital image correlation. Materials and Structures, 2015, 48(8): 2713−2726
12. Hamrat M, Boulekbache B, Chemrouk M, Amziane S. Flexural cracking behavior of normal strength, high strength and high strength fiber concrete beams, using digital image correlation technique. Construction & Building Materials, 2016, 106: 678−692
13. Bencardino F, Rizzuti L, Spadea G, Swamy R N. Stress−strain behavior of steel fiber-reinforced concrete in compression. Journal of Materials in Civil Engineering, 2008, 20(3): 255−263
14. Yazıcı Ş, İnan G, Tabak V. Effect of aspect ratio and volume fraction of steel fiber on the mechanical properties of SFRC. Construction & Building Materials, 2007, 21(6): 1250−1253
15. Yoo D Y, Yoon Y S, Banthia N. Flexural response of steel-fiber-reinforced concrete beams: Effects of strength, fiber content, and strain-rate. Cement and Concrete Composites, 2015, 64: 84−92
16. Thomas J, Ramaswamy A. Mechanical properties of steel fiber-reinforced concrete. Journal of Materials in Civil Engineering, 2007, 19(5): 385−392
17. Taerwe L R. Influence of steel fibers on strain-softening of high-strength concrete. ACI Materials Journal, 1993, 89(1): 54−60
18. Katzer J, Domski J. Quality and mechanical properties of engineered steel fibres used as reinforcement for concrete. Construction & Building Materials, 2012, 34: 243−248
19. Han J, Zhao M, Chen J, Lan X. Effects of steel fiber length and coarse aggregate maximum size on mechanical properties of steel fiber reinforced concrete. Construction & Building Materials, 2019, 209: 577−591
20. Abdallah S, Fan M. Anchorage mechanisms of novel geometrical hooked-end steel fibres. Materials & Structures, 2017, 50(2): 139
21. Ng T S, Foster S J, Htet M L, Htut T N S. Mixed mode fracture behaviour of steel fibre reinforced concrete. Materials and Structures, 2014, 47(1−2): 67−76
22. Abdallah S, Rees D W, Ghaffar S H, Fan M. Understanding the effects of hooked-end steel fibre geometry on the uniaxial tensile behaviour of self-compacting concrete. Construction & Building Materials, 2018, 178: 484−494
23. Elmenshawi A, Brown T. Hysteretic energy and damping capacity of flexural elements constructed with different concrete strengths. Engineering Structures, 2010, 32(1): 297−305
24. Daniel L, Loukili A. Behavior of high strength fiber-reinforced concrete beams under cyclic loading. ACI Structural Journal, 2002, 99(3): 248−256
25. Boulekbache B, Hamrat M, Chemrouk M, Amziane S. Flexural behaviour of steel fibre-reinforced concrete under cyclic loading. Construction & Building Materials, 2016, 126: 253−262
26. Chalioris C E, Kosmidou P K, Karayannis C G. Cyclic response of steel fiber reinforced concrete slender beams: An experimental study. Materials (Basel), 2019, 12(9): 1398
27. Naghibdehi M G, Naghipour M, Rabiee M. Behaviour of functionally graded reinforced-concrete beams under cyclic loading. Gradevinar, 2015, 67(5): 427−439
28. Ganesan N, Indira P, Sabeena M. Behaviour of hybrid fibre reinforced concrete beam–column joints under reverse cyclic loads. Materials & Design, 2014, 54: 686−693
29. Radtke F, Simone A, Sluys L. A computational model for failure analysis of fibre reinforced concrete with discrete treatment of fibres. Engineering Fracture Mechanics, 2010, 77(4): 597−620
30. Cunha V M, Barros J A, Sena-Cruz J. An integrated approach for modelling the tensile behaviour of steel fibre reinforced self-compacting concrete. Cement and Concrete Research, 2011, 41(1): 64−76
31. Bitencourt L A Jr, Manzoli O L, Bittencourt T N, Vecchio F J. Numerical modeling of steel fiber reinforced concrete with a discrete and explicit representation of steel fibers. International Journal of Solids and Structures, 2019, 159: 171−190
32. Huo L, Bi J, Zhao Y, Wang Z. Constitutive model of steel fiber reinforced concrete by coupling the fiber inclining and spacing effect. Construction & Building Materials, 2021, 280: 122423
33. Chi Y, Xu L, Yu H. Constitutive modeling of steel-polypropylene

hybrid fiber reinforced concrete using a non-associated plasticity and its numerical implementation. Composite Structures, 2014, 111: 497−509

34. Luccioni B, Ruano G, Isla F, Zerbino R, Giaccio G. A simple approach to model SFRC. Construction & Building Materials, 2012, 37: 111−124
35. Roesler J, Paulino G H, Park K, Gaedicke C. Concrete fracture prediction using bilinear softening. Cement and Concrete Composites, 2007, 29(4): 300−312
36. Association C S. Canadian Highway Bridge Design Code (CHBDC)-Fiber Reinforced Concrete: Annex 8.1 of CSA-S6. 2018
37. Kosmatka S, Kerkhoff B, McGrath R, Hooton R. Design and Control of Concrete Mixtures, eighth Canadian Edition. Ottawa: Cement Association of Canada, 2011
38. Standard ASTM, C39/C39M-20. Standard Test Method for Compressive Strength of Cylindrical Concrete Specimens. West Conshohocken: ASTM International, 2020
39. Standard ASTM, C469/C469M-14. Standard Test Method for Static Modulus of Elasticity and Poisson's ratio of Concrete in Compression. West Conshohocken: ASTM International, 2014
40. Standard ASTM, C496/C496M-17. Standard Test Method for Splitting Tensile Strength of Cylindrical Concrete Specimens. West Conshohocken: ASTM International, 2017
41. Standard ASTM, C1609/C1609M-19. Standard Test Method for Flexural Performance of Fiber-reinforced Concrete (Using Beam with Third-point Loading). West Conshohocken: ASTM International, 2019
42. Boulekbache B, Hamrat M, Chemrouk M, Amziane S. Influence of yield stress and compressive strength on direct shear behaviour of steel fibre-reinforced concrete. Construction & Building Materials, 2012, 27(1): 6−14
43. Lee S C, Oh J H, Cho J Y. Compressive behavior of fiber-reinforced concrete with end-hooked steel fibers. Materials (Basel), 2015, 8(4): 1442−1458
44. Nataraja M, Dhang N, Gupta A. Stress–strain curves for steel-fiber reinforced concrete under compression. Cement and Concrete Composites, 1999, 21(5−6): 383−390
45. Ou Y C, Tsai M S, Liu K Y, Chang K C. Compressive behavior of steel-fiber-reinforced concrete with a high reinforcing index. Journal of Materials in Civil Engineering, 2012, 24(2): 207−215
46. Krenchel H. Fibre Spacing and Specific Fibre Surface. Fibre Reinforced Cement and Concrete. Lancaste: The Construction Press, 1975
47. Soroushian P, Lee C D. Distribution and orientation of fibers in steel fiber reinforced concrete. ACI Materials Journal, 1990, 87(5): 433−439
48. Dupont D, Vandewalle L. Distribution of steel fibres in rectangular sections. Cement and Concrete Composites, 2005, 27(3): 391−398
49. Matzenmiller A, Lubliner J, Taylor R L. A constitutive model for anisotropic damage in fiber-composites. Mechanics of Materials, 1995, 20(2): 125−152
50. Ren X, Li J. Multi-scale based fracture and damage analysis of steel fiber reinforced concrete. Engineering Failure Analysis, 2013, 35: 253−261
51. Corporation D S S. Manual, ABAQUS User. 6.10-EF, 2010
52. Menna D W, Genikomsou A S. Punching shear response of concrete slabs strengthened with ultrahigh-performance fiber-reinforced concrete using finite-element methods. Practice Periodical on Structural Design and Construction, 2021, 26(1): 04020057
53. Wahalathantri B, Thambiratnam D, Chan T, Fawzia S. A material model for flexural crack simulation in reinforced concrete elements using ABAQUS. In: Proceedings of the First International Conference on Engineering, Designing and Developing the Built Environment for Sustainable Wellbeing. Brisbane: Queensland University of Technology, 2011, 260−264
54. Kanakubo T. Tensile characteristics evaluation method for ductile fiber-reinforced cementitious composites. Journal of Advanced Concrete Technology, 2006, 4(1): 3−17
55. R. TC162-TDF. Test and design methods for steel fibre reinforced concrete: Uniaxial tension test for steel fibre reinforced concrete. Materials and Structures, 2001, 34: 3−6
56. Abrishambaf A, Barros J A, Cunha V M. Tensile stress–crack width law for steel fibre reinforced self-compacting concrete obtained from indirect (splitting) tensile tests. Cement and Concrete Composites, 2015, 57: 153−165
57. López J Á, Serna P, Navarro-Gregori J, Coll H J C P B E. A simplified five-point inverse analysis method to determine the tensile properties of UHPFRC from unnotched four-point bending tests. Composites. Part B, Engineering, 2016, 91: 189−204
58. Gao D, Ding C, Pang Y, Chen G. An inverse analysis method for multi-linear tensile stress-crack opening relationship of 3D/4D/5D steel fiber reinforced concrete. Construction & Building Materials, 2021, 309: 125074
59. Ralli Z G, Genikomsou A S, Pantazopoulou S J. Comparative evaluation of nonlinear FEA inverse analysis of tensile properties of UHPFRC. In: FIB Symposium 2021 Concrete Structures: New Trends for Eco-Efficiency and Performance. Lisbon: International Federation for Structural Concrete, 2021
60. Yang Y, Massicotte B, Genikomsou A S, Pantazopoulou S J, Palermo D. Comparative investigation on tensile behaviour of UHPFRC. Materials and Structures, 2021, 54(4): 147
61. Genikomsou A S, Polak M A. Finite element analysis of punching shear of concrete slabs using damaged plasticity model in ABAQUS. Engineering Structures, 2015, 98: 38−48